Article

Radiative forcing reduced by early twenty-first century increase in land albedo

https://doi.org/10.1038/s41586-025-08987-z

Received: 15 May 2024

Accepted: 4 April 2025

Published online: 28 May 2025

Check for updates

Zhengyang Hou[1], Liqiang Zhang[1,2]✉, Jingjing Peng[3], Giovanni Forzieri[4], Aolin Jia[5], Zhiqiang Xiao[1], Ying Qu[1], Jintai Lin[6,7]✉, Duoying Ji[1], Zidong Zhu[1], Xin Yao[1], Shuwen Peng[1], Lanpu Zhao[2], Wenjie Fan[8], Zhaocong Wu[2], Hao Geng[1], Qihao Wang[1], Chenghu Zhou[9]✉, Suhong Liu[1] & Liangpei Zhang[2]✉

Surface albedo greatly affects how much energy the Earth absorbs. Intensive human activities and accelerated climate change have altered surface albedo across spatial and temporal scales[1–3], yet assessments of the effects of land use or land cover (LULC) and snow variations on land surface albedo are scarce at the global scale. As a result, the global land surface albedo dynamics over recent decades and their corresponding radiative forcing to the climate system remain poorly understood[4–9]. Here we quantify the individual and combined effects of snow cover dynamics, LULC conversions and non-conversion regions on albedo variations during 2001–2020 and estimate their induced radiative forcing. We show that the negative radiative forcing induced by the global land surface albedo change was −0.142 (−0.158, −0.114) W m^{-2} over the past two decades. The global snow-free land surface albedo increased by 2.2% ($P < 0.001$), with a negative radiative forcing of −0.164 (−0.186, −0.138) W m^{-2} ($P < 0.001$). The magnitude of this negative forcing is sevenfold larger than the positive forcing induced by snow dynamics, and equivalent to 59.9% of that caused by CO_2 emissions from 2011 to 2019[10]. The global radiative forcing due to albedo changes in LULC non-conversion regions is 3.9 to 8.1 times greater than that from LULC conversions. The radiative forcing induced by albedo changes highlights the important role of land surface dynamics in modulating global warming.

Land surface albedo modulates the amount of energy that the Earth absorbs from the Sun, and it is thus a key variable influencing surface temperature and water balance[11–15]. The anthropogenic intensification of land use or land cover (LULC) and the continuing climate change are profoundly altering landscape characteristics and land physical processes, ultimately causing large changes in surface albedo[1–3], which directly alter the Earth's radiation budget. LULC conversions, for instance associated with the increasing urbanization and widespread deforestation can abruptly change surface reflectance properties and thus their albedo. The LULC non-conversion regions may also experience important albedo variations due to long-term processes such as the browning and/or greening and wetting and/or dying of natural ecosystems, and short-term processes such as the recurrent changes induced by phenological stages and crop rotation[16]. Owing to the disparities of land-climate interactions among the regions, even the same LULC types may have different albedo across regions[17]. The complexity of these processes acting at different spatial and temporal scales, coupled with data and methodological gaps in observing such dynamics, makes it challenging to quantify the variations in global land albedo and their climate impact.

Satellite data allow for systematic tracking of spatial and temporal albedo dynamics[18] and have been widely used for global surface energy budget assessments[19–22]. However, existing albedo products face substantial data gaps, primarily because of cloud contamination in optical satellite imagery used for albedo retrieval, especially in persistently cloudy regions such as the Amazonian forests[23–25]. Accurately estimating missing albedo values requires accounting for the LULC types and the discontinuity of surface albedo over space and time due to LULC differences.

Accounting for the heterogeneous albedo effects from varying land surface properties is crucial as they drive distinct radiative forcing. Previous studies have primarily focused on specific LULC types or human driven type-to-type conversions and their effects on albedo and radiative forcing[4–9]. However, these studies, failing to explore the full range of LULC conversions and snow dynamics, can only provide a partial quantification of surface albedo. Moreover, 63.5–68.5% of the global land surface does not undergo LULC conversions, but the changes in surface albedo over these non-conversion regions and their corresponding climate effects have been so far poorly explored. As a

[1]State Key Laboratory of Remote Sensing and Digital Earth, Faculty of Geographical Science, Beijing Normal University, Beijing, China. [2]Aerospace Information Research Institute, Henan Academy of Sciences, Zhengzhou, China. [3]Earth System Science Interdisciplinary Center/Cooperative Institute for Satellite Earth System Studies (CISESS), University of Maryland, College Park, MD, USA. [4]Department of Civil and Environmental Engineering, University of Florence, Florence, Italy. [5]Remote Sensing and Natural Resource Modeling, Department ERIN, Luxembourg Institute of Science and Technology, Belvaux, Luxembourg. [6]Laboratory for Climate and Ocean-Atmosphere Studies, Department of Atmospheric and Oceanic Sciences, School of Physics, Peking University, Beijing, China. [7]Institute of Carbon Neutrality, Peking University, Beijing, China. [8]School of Earth and Space Sciences, Peking University, Beijing, China. [9]State Key Laboratory of Resources and Environmental Information System, Institute of Geographical Science and Natural Resources, Chinese Academy of Sciences, Beijing, China. ✉e-mail: zhanglq@bnu.edu.cn; linjt@pku.edu.cn; zhouch@lreis.ac.cn; zlp62@whu.edu.cn

result, how LULC and snow dynamics have driven the observed global land surface albedo and influenced the surface energy budget over the past decades is still lacking so far.

Here we conduct a comprehensive analysis of global land surface albedo dynamics and resulting global radiative forcing over the period 2001–2020. We quantify the contributions from snow dynamics, LULC conversions and non-conversion regions on the basis of 612 conversion pathways across 50 LULC types in four LULC classification schemes. We integrate the 500-m-resolution MODIS-based albedo[18], snow cover[26] and LULC[27] products in a consistent multi-dimensional array. Albedo and LULC conversions are then aggregated at 1° × 1° spatial resolution and at monthly scale separately for each LULC type, and the four-dimensional spatio-temporal inverse distance weighted (IDW) interpolation model is used to reconstruct missing data. From this, we generate four seamless monthly albedo and land cover look-up maps (ALLUMs) from 2001 to 2020 (Extended Data Fig. 1a and Methods), each corresponding to one of the four LULC classification schemes. ALLUMs are used to explain how snow dynamics, LULC conversions and LULC non-conversion regions individually influence global land surface albedo changes. We also use six radiative forcing kernels to quantify the global land surface mean radiative forcing over the past two decades. Finally, we integrate photosynthetic vegetation (PV), non-photosynthetic vegetation (NPV) and surface water content (SWC) within a multivariate linear regression framework to uncover the mechanisms driving albedo variations in non-conversion regions.

ALLUM datasets

The ALLUM multi-dimensional arrays, each one separately generated from the four reference classification schemes, provided white-sky and black-sky albedo in three bands for all 50 LULC types excluding water bodies, as well as for all 612 LULC conversion regions and 50 non-conversion regions within each 1° × 1° grid cell. Missing albedo data were reconstructed using a four-dimensional spatio-temporal IDW model (Supplementary Text 1). The filling method shows $r^2 \geq 0.98$ and root mean square error (r.m.s.e.) ≤ 0.035 across the three bands over the four ALLUMs (Supplementary Figs. 1–3, details in Methods). The four sets of the reconstructed 500-m-resolution albedo based on the four ALLUMs align closely with the monthly average albedo from MCD43A3, with $r^2 \geq 0.96$ and an r.m.s.e. ≤ 0.050 (Extended Data Fig. 1b, Supplementary Figs. 4 and 5 and Methods) for latitudes with solar zenith angles below 70°. Such results confirm that the ALLUMs are suitable for investigating global land surface albedo changes on a monthly timescale.

Global land surface albedo change

The global snow-free land surface albedo (GSLA) (that is, in the snow-free regions that were not covered by snow in the same months of both 2001 and 2020) increased by 2.2%. This corresponds to an absolute change of 0.0038 (0.0036, 0.0039) (t-test, $P < 0.001$) and a significant trend of 0.0011 per decade (Mann–Kendall test, $P = 0.048$; Fig. 1a and Extended Data Fig. 2), which represents the average annual albedo change derived from the four ALLUMs (Methods) with upper and lower limits indicating the maximum and minimum values of the albedo change in four seasons of each year. This increase raised the global land surface mean albedo by 0.0031 (Fig. 1d), which offset the decline in global land surface mean albedo caused by the snow albedo change and the widespread reduction in snow cover (−0.0013, Fig. 1e). As a result, the global land surface mean albedo in 2020 was 0.72% higher than that in 2001 (0.0018 (0.0006, 0.0029); t-test, $P < 0.001$; Fig. 1a–c). However, the interannual fluctuations made the trend statistically insignificant (Fig. 1a). Snow cover changes were the primary driver of these fluctuations (Supplementary Text 2) due to higher albedo of snow compared to other LULC types, as seen in peaks in 2009, 2016 and 2018. This was also reflected in the high correlation (Pearson's $r = 0.91$) between snow areas and global land surface mean albedo after detrending (Fig. 1a).

To verify the robustness of our results, albedo change estimates derived from ALLUMs were confronted with analogous estimates retrieved from independent satellite-based products and in situ observations (Supplementary Text 3, Extended Data Fig. 3 and Supplementary Figs. 6–11). We further validated the sensitivity of our results (Supplementary Fig. 12) as well as MODIS instrument calibration errors (Supplementary Text 4, Extended Data Fig. 4 and Supplementary Figs. 13 and 14), demonstrating the robustness of the methods and the validity of our findings. Notably, the trends in albedo estimated at the local scale falling below the calibration limit were associated with uncertainties[28], particularly in polar regions covered with snow and ice (these regions were highlighted in Supplementary Fig. 15).

We found a considerable spatial variability in surface albedo change. In the northern temperate zone, the average albedo of snow-free regions increased by 1.20% (0.0021 (0.0018, 0.0027); Extended Data Fig. 2 and Extended Data Fig. 5a), but overall (snow and snow-free) albedo remained almost unchanged due to the snow-melt induced decreases (Extended Data Fig. 5b). At high northern latitudes, such as northern Asia, there was a marked decline in albedo (Fig. 1c). Similarly, evergreen needleleaf forests in eastern Europe experienced a decline, while eastern Canadian plain experienced an increase. By contrast, snow dynamics had no obvious effects on albedo changes in the tropical regions and very marginally in southern temperate regions (Extended Data Fig. 5b versus Extended Data Fig. 5a). In the tropical regions, albedo increased by 0.0034 (0.0027, 0.0039) (Extended Data Fig. 5b). Increases in albedo also occurred over grasslands, savannas and barren lands in Africa and South America. In the southern temperate zones, albedo increased by 9.5% (0.0150 (0.0117, 0.0188); Extended Data Fig. 5b), especially over Australia, southern Africa and South America (Fig. 1c). However, albedo decreased over equatorial evergreen broadleaf forests and croplands in the Indian Peninsula.

The changes in snow-free albedo in the northern and southern temperate regions and tropical regions drove the GSLA increase over the past 20 years (Extended Data Fig. 5b). Notably, only the increase in tropical albedo showed a stable linear trend from 2001 to 2020 (0.0013 per decade for trend, Mann–Kendall test, $P = 0.0016$; Extended Data Fig. 5b), whereas the GSLA during 2009–2011 and 2011–2016 were primarily driven by decreases in albedo in the southern and northern temperate zones, respectively.

The induced radiative forcing

To calculate the global mean radiative forcing induced by surface albedo changes, we used 2001 as baseline value and computed the changes in global mean radiative forcing from 2001 to 2020 using six radiative kernels. These kernels estimated the net shortwave radiative flux change at the top of the atmosphere (Methods). The maximum and minimum values of radiative forcing derived from these kernels and the four ALLUMs were then used to quantify the uncertainty range (Methods).

The global mean radiative forcing due to the GSLA change from 2001 to 2020 was −0.164 (−0.186, −0.138) W m^{-2} (t-test, $P < 0.001$), and showed a significant trend of −0.0427 W m^{-2} per decade for trend (Mann–Kendall test, $P = 0.0010$; Fig. 2a,d). The magnitude of the forcing was about 59.9% of the CO_2 radiative forcing and 48.9% of the total greenhouse gas forcing from 2011 to 2019 (IPCC Sixth Assessment Report (AR6))[10], but with the opposite sign. When including albedo reductions caused by snow dynamics, the global mean radiative forcing for the same period was −0.142 (−0.158, −0.114) W m^{-2} (t-test, $P < 0.001$; Fig. 2a–c). Although snow dynamics caused greater interannual fluctuations in global mean radiative forcing, they did not diminish the significance of the trend (−0.0404 W m^{-2} per decade, Mann–Kendall test, $P = 0.0478$; Fig. 2a and Supplementary Text 2). Furthermore, the

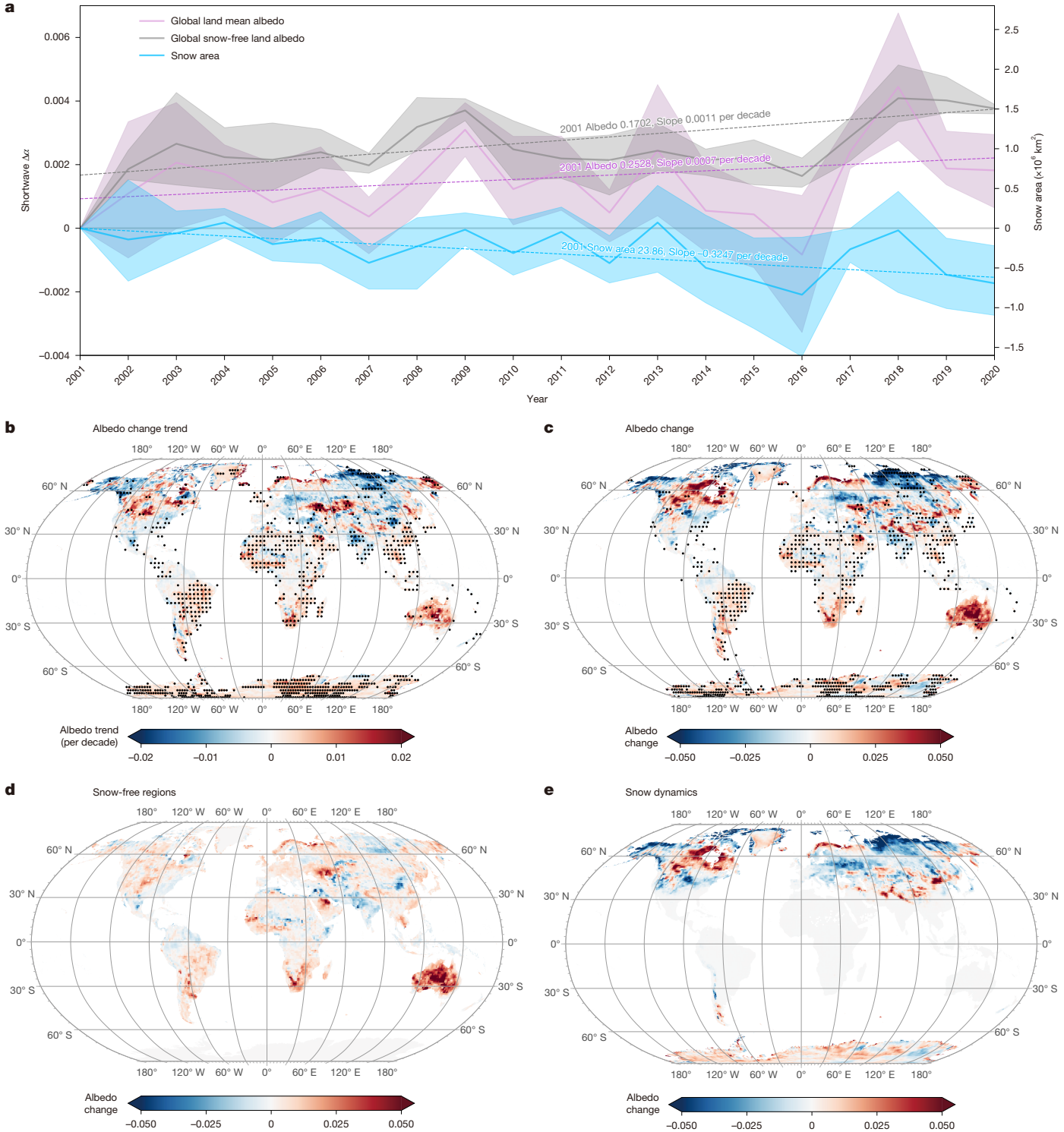

Fig. 1 | Changes in global land surface albedo from 2001 to 2020. a, Annual time series of global land surface mean albedo (purple), GSLA (grey) and snow cover area (blue), with dashed lines representing linear fits using the Theil–Sen Median method as a robust statistical approach. Shaded areas show maximum and minimum values of albedo change of the four seasons using the four ALLUMs. **b**, Spatial distribution of the 20-year global land surface albedo change trend. The Theil–Sen Median method is used to retrieve linear trends at the grid-cell level. Black dots represent the regions with statistically significant trends, determined by the Mann–Kendall test ($P < 0.05$). The regions with statistically significant trends account for 31.0% of the global land area (23.8% showing an increase and 7.2% showing a decrease). **c**, Spatial distribution of albedo changes between 2001 and 2020. The black dots indicate the bins in which the average albedo change between two independent temporal windows (2011–2020 and 2001–2010) is statistically significant (different from zero in two-sided Student's *t*-test; $P < 0.05$). The regions with statistically significant changes account for 26.8% of the global land area (19.1% showing an increase and 7.7% showing a decrease). **d**,**e**, Spatial distribution of mean albedo changes in each 1° × 1° grid cell attributed to the snow-free regions (**d**) and snow dynamics (**e**). These results are the averages calculated from ALLUM-LCCS 1–3 and ALLUM-IGBP. Significance tests for **b** and **c** are conducted within each 3° × 3° grid cell for visual purposes.

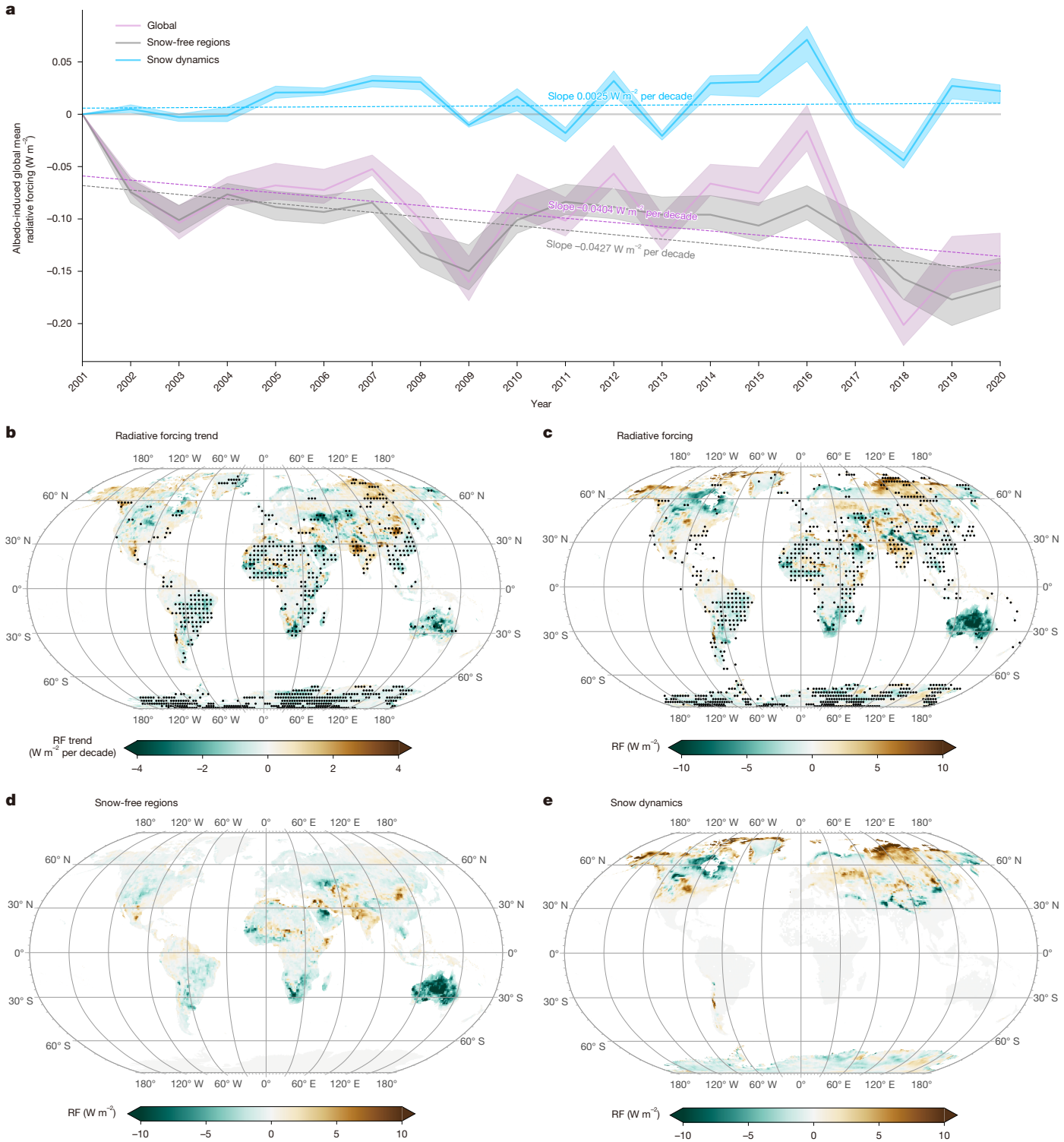

Fig. 2 | Albedo-induced radiative forcing from 2001 to 2020. a, Global mean radiative forcing averaged across six radiative kernels and the four ALLUMs induced by the global land surface mean albedo change (purple), GSLA change (grey) and snow dynamics (blue). Dashed lines represent the linear fits using the Theil–Sen Median method as a robust statistical approach. The shaded area represents the ranges of the maximum and minimum values of the radiative forcing. **b**, Spatial distribution of 20-year global land albedo-induced radiative forcing (RF) trend. The Theil–Sen Mdeian method is used to retrieve linear trends at the grid-cell level. Black dots represent the regions with statistically significant trends, as determined by the Mann–Kendall test ($P < 0.05$). The regions with statistically significant trends account for 32.4% of the global land area (7.0% showing an increase and 25.4% showing a decrease). **c**, Spatial distribution of grid-mean radiative forcing induced by albedo changes. Black dots indicate the bins in which the average albedo-induced radiative forcing change between two time periods (2011–2020 and 2001–2010) is statistically significant (different from zero in a two-sided Student's *t*-test; $P < 0.05$). The regions with statistically significant changes account for 28.2% of the global land area (7.6% showing an increase and 20.6% showing a decrease). **d**,**e**, Spatial distribution of grid-mean radiative forcing induced by snow-free land surface change (**d**) and snow dynamics (**e**) during 2001–2020. Significance tests for **b** and **c** are conducted within each 3° × 3° grid cell for visual purposes.

integrated radiative forcing, used to quantify the change of absorbed shortwave radiation energy due to the global land surface mean albedo change, indicated a decrease of 2.958 (2.320, 3.363) × 10^{22} J in absorbed energy from 2002 to 2020.

Attributions of albedo and radiative forcing

LULC conversions often triggered substantial surface albedo changes, as albedo showed large disparities across different LULC types[4,6,8]. There were considerable variations in the areas and extents of LULC conversion regions across the four classification schemes due to the differences in the definition and number of LULC types (Fig. 3 and Supplementary Figs. 16–18). Water bodies were excluded from the analysis in all classification schemes. The three classification schemes LCCS 1–3 (Food and Agricultural Organization Land Cover Classification System (LCCS) 1–3, refs. 29,30) separately provided 15, 10 and 9 LULC types (Supplementary Tables 1–3), and were designed to characterize for different applications. The IGBP (International Geosphere-Biosphere Programme[31]) scheme contained 16 widely used LULC types (Supplementary Table 4). Over the snow-free regions, there were 9–16 LULC types and 72–240 LULC conversion pathways depending on the LULC classification schemes (Fig. 3b and Supplementary Figs. 16b, 17b and 18b). The snow-free LULC conversion regions contributed to 12.6–22.1% of the GSLA change from 2001 to 2020 (Fig. 4a, Extended Data Fig. 6 and Methods). The snow-free regions with LULC non-conversions covered 78.6–84.9% of global snow-free land surface and contributed to 77.9–87.4% of the GSLA change and increased the global land surface mean albedo by 0.0024–0.0027.

During 2001–2020, the global mean radiative forcing from albedo changes in LULC non-conversion regions was 3.9 to 8.1 times larger than the forcing caused by LULC conversions (−0.131 (−0.146, −0.111) W m^{-2} versus −0.0333 (−0.0390, −0.0275) W m^{-2} for the smallest difference in LCCS 1, and −0.1455 (−0.163, −0.123) W m^{-2} versus −0.0179 (−0.0213, −0.0143) W m^{-2} for the largest difference in IGBP; Fig. 4b, Extended Data Fig. 7 and Methods). The radiative forcing by the non-conversion regions over this 20-year period was comparable to the forcing induced by anthropogenic LULC conversions over the past three centuries (−0.15 ± 0.1 W m^{-2}, IPCC AR6, ref. 10). On the basis of our results, the radiative forcing of LULC conversions from 2001 to 2020 through the pathways caused by human activities was −0.0101 (−0.0119, −0.0081) W m^{-2}, with a reduction rate of 0.0053 (0.0043, 0.0063) W m^{-2} per decade. Our estimate was largely consistent with the value of −0.0056 W m^{-2} per decade over the period 1750–2019 reported in the IPCC AR6 (ref. 10) (Supplementary Text 5).

In each of the four LULC classification schemes, the contribution of snow cover conversions to the global land surface mean albedo change was represented by all snow-related LULC conversion pathways, which included the conversions from snow cover to other non-snow LULC types and vice versa. Snow dynamics, including snow cover conversions and snow albedo changes in snow-covered non-conversion regions, contributed to a global land surface mean albedo decrease, but its magnitude was only 41.4% of the GSLA increase (−0.0013 versus 0.0031; Figs. 1e and 4a). The snow dynamics-associated global land surface mean albedo decline was primarily driven by snow cover reduction, with the contribution of snow albedo changes less than 0.0001 (Fig. 5a and Supplementary Figs. 19a, 20a and 21a. Supplementary Fig. 22 illustrates the snow albedo change at the 1° grid-cell spatial resolution). The radiative forcing resulting from snow dynamics was only 0.0222 (0.0105, 0.0280) W m^{-2}, equivalent to −13.5% of the radiative forcing caused by the GSLA increase (Figs. 2a,d and 4b).

Among the four classification schemes, the LCCS 2 contained many key LULC types, including cropland, urban areas, shrublands, natural herbaceous, dense forests and open forests, and showed a relatively high classification accuracy (81% of overall accuracy) across four classification schemes[32]. Under LCCS 2, the albedo changes from LULC conversions and non-conversion regions separately led to a global land surface mean albedo increase of 0.0005 and 0.0026 (15.8 and 84.2% of GSLA, Fig. 4a), resulting in radiative forcing of −0.0239 (−0.0283, −0.0195) and −0.141 (−0.157, −0.120) W m^{-2} (14.6 and 85.9% of GSLA radiative forcing, Fig. 4b). Results obtained for the other classification schemes were similar as shown in Supplementary Figs. 16–18 and 19–21.

Under the LCCS 2 scheme, there were 36 net bidirectional LULC conversions among nine non-snow LULC types from 2001 to 2020 (Fig. 5). Results for other classification schemes are shown in Supplementary Figs. 19–21. Among the 36 net conversions, shrublands and open forests converted to natural herbaceous areas were about 157,862 and 561,554 km^2, respectively (Fig. 3b). These two pathways contributed the most to the GSLA increase (5.4 and 5.3%) and global radiative forcing (−0.0091 and −0.0087 W m^{-2}). The second largest contribution came from the net conversion from dense forests to open forests (254 km^2), accounting for a 3.8% increase in GSLA and −0.0056 W m^{-2} of radiative forcing. Barren lands were mainly converted in net to natural herbaceous and shrublands (Fig. 3b), contributing to −2.5 and −1.2% of the GSLA change, with radiative forcing of 0.0053 and 0.0023 W m^{-2}.

The classification of mixed cropland LULC types (forest and/or cropland mosaics and natural herbaceous and/or cropland mosaics) introduced a large uncertainty to the delineation of cropland regions, because the areal fraction of croplands was unknown. Thus, under the LCCS 2 scheme, we calculated the effects of cropland changes on albedo and radiative forcing under two scenarios (one considering only herbaceous cropland as cropland, and the other one considering both herbaceous cropland and mixed cropland LULC types as cropland). Results of these two experiments were then used as the upper and lower bounds of the uncertainty range. From 2001 to 2020, the global cropland-relative conversions contributed to 2.4–3.7% of the GSLA increase (Fig. 4a), with induced radiative forcing of (−0.0057)–(−0.0039) W m^{-2} (Fig. 5b).

Urban expansion under LCCS 2 contributed to less than 0.1% of the GSLA increase with radiative forcing less than 0.0001 W m^{-2}. When the conversions between urban and snow were also included, the radiative forcing induced by urban expansion during 2001 and 2018 aligned with previous estimates (0.00013 W m^{-2} for ALLUM-LCCS 2 and 0.00015 W m^{-2} for ALLUM-IGBP compared to 0.00017 W m^{-2} in ref. 4).

In the LULC non-conversion regions under LCCS 2, non-snow LULC types (except natural herbaceous and/or cropland mosaic, which covered less than 0.1% of the global snow-free land area) experienced varying degrees of albedo increase (Fig. 3a). Shrublands showed the highest albedo increase (by 0.0151), contributed the most to the GSLA change (31.9%, Fig. 5a) and global mean radiative forcing (35.5%, Fig. 5b). Natural herbaceous areas, covering the largest fraction of snow-free land (17.9%), had the second highest albedo increase (0.0051) contributing to 24.0 and 22.9% of GSLA change and radiative forcing, respectively. Meanwhile, about 12.0, 7.7 and 7.1–7.6% (on the basis of the above mentioned two scenarios) of the GSLA increase were attributed to open forests, barren and croplands, respectively. Dense forests showed the smallest albedo increase (less than 0.2%).

The albedo changes in LULC non-conversions regions under the other three classification schemes (Supplementary Figs. 16a, 17a and 18a) were similar to those retrieved for the LCCS 2 scheme. For instance, shrublands and short natural vegetation types (natural herbaceous, grasslands and savannas) showed the largest albedo increase consistently across all schemes.

Overall, the albedo enhancement in non-barren LULC non-conversion regions under LCCS 2 increased global land surface mean albedo by 0.0024, contributing to 76.6% of the GSLA increase and resulted in a global mean radiative forcing of −0.126 (−0.141, −0.107) W m^{-2}, accounting for 76.4% of GSLA-induced forcing. The albedo changes in

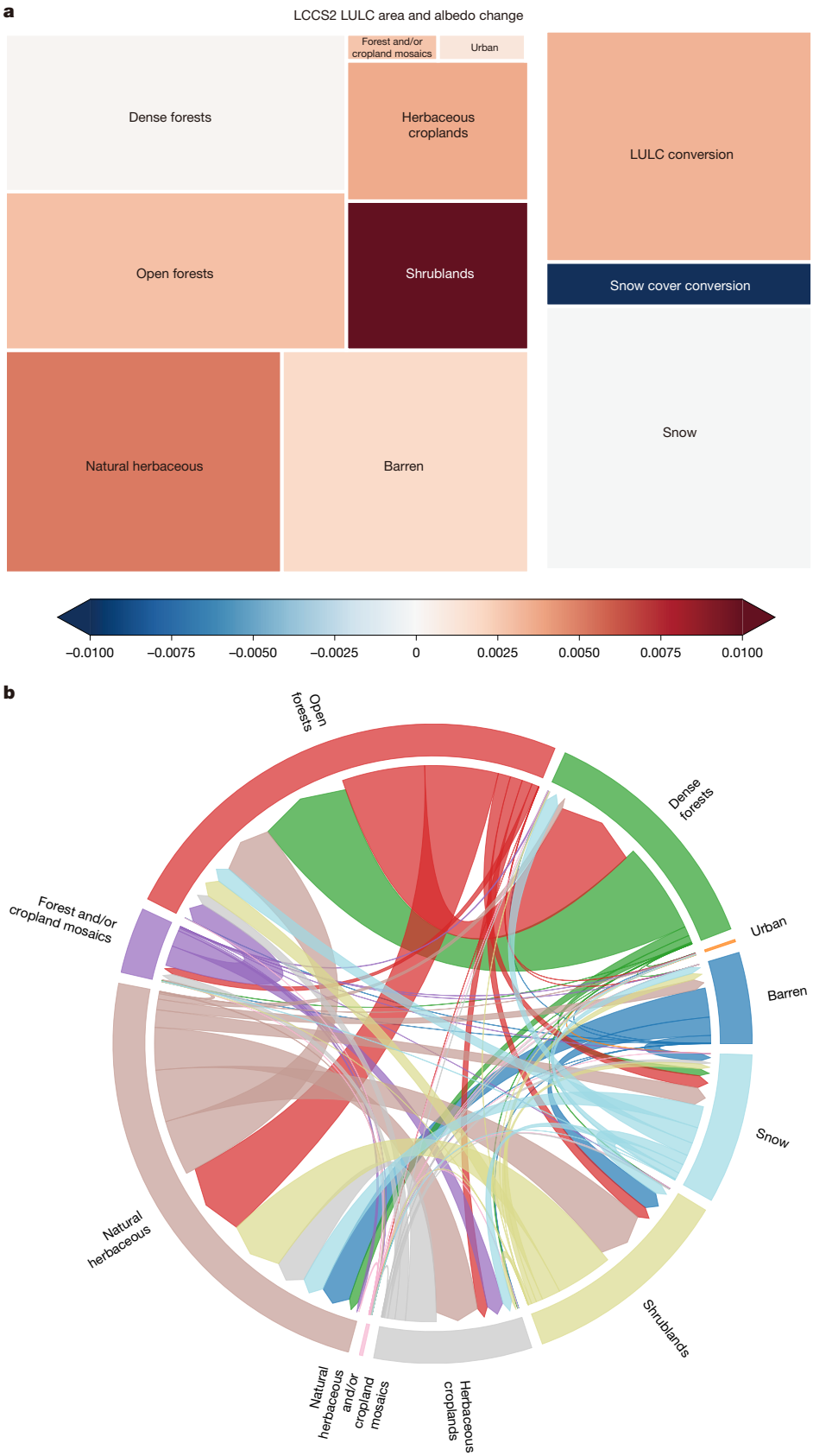

Fig. 3 | Global LULC and albedo changes under LCCS 2. a, Albedo changes across all regions with and without LULC conversions defined by LCCS 2. The area of each rectangle represents the proportion of land occupied by each specific LULC type, and the colour indicates the albedo change. Natural herbaceous and/or cropland mosaics are invisible due to their small areas (less than 0.1% of the global land area). **b**, Areas of LULC changes through 90 conversion pathways. The arc length represents the area of LULC conversion regions associated with the corresponding LULC type *t*. Inward arrows show conversions from other LULC types to *t*, and outward arrows indicate conversions from *t* to other types. The thickness of the arrows reflects the size of the conversion area.

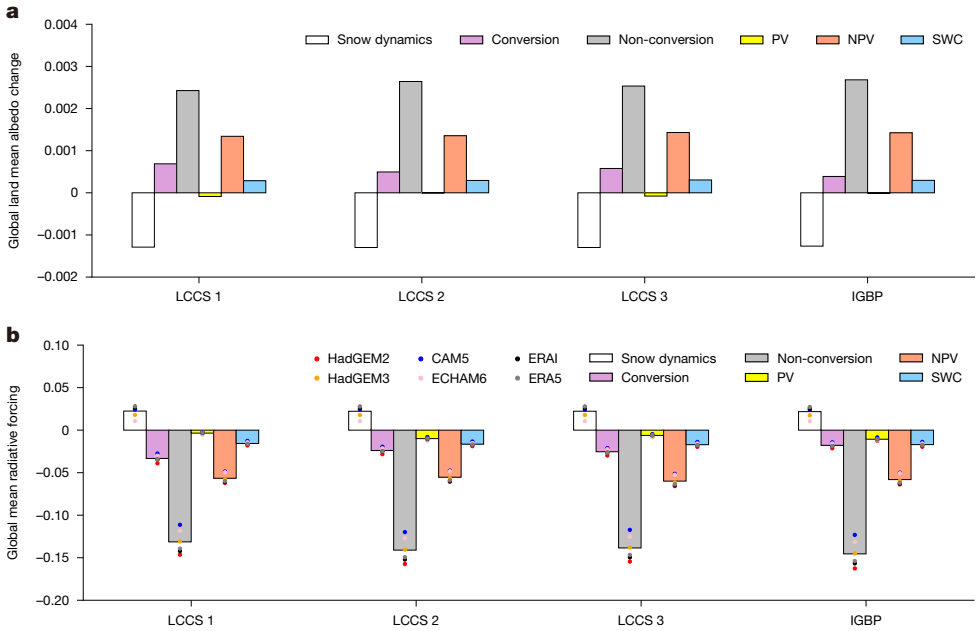

Fig. 4 | Albedo change and resulting forcing. a, Global land surface mean albedo changes induced by different factors under the four LULC classification schemes. **b**, Albedo-induced global mean radiative forcing. White, purple and grey bars represent albedo changes due to snow dynamics, LULC conversions and those in LULC non-conversion regions, respectively. Green, orange and blue bars represent the individual contributions of PV, NPV and SWC. The points in **b** represent the global mean radiative forcing calculated from six different radiative kernels.

these non-barren, non-conversion regions could be largely explained by changes in PV, NPV and SWC. PV refers to plant types actively engaged in photosynthesis, such as green leaves and grasses. NPV includes plant components that do not photosynthesize, such as dry leaves, stems and woody material, commonly found in shrubs and dead plant matter[33]. SWC represents the amount of water in soil or vegetation surface, which influences albedo by altering the reflectivity of the surface[34].

As such, we used a PV-NPV-SWC multivariate linear regression model to assess their effects on GSLA by fitting albedo changes at monthly and pixel scales (Extended Data Fig. 1c and Methods). In regions with solar zenith angles less than 85°, r^2 of the model for predicting white- and black-sky albedo were 0.931 and 0.943, respectively, with r.m.s.e. values of 0.0102 and 0.0090 (Supplementary Fig. 23 and Methods). On the basis of this model, changes in PV, NPV and SWC led to an estimated global land surface mean albedo increase of 0.0016. This increase was 52.9% of the actual GSLA increase, or 68.5% of the surface albedo variations in non-barren, non-conversion regions. The estimated albedo change from the PV-NPV-SWC model led to radiative forcing of −0.0818 (−0.0914, −0.0689) W m^{-2}, explaining 49.8% of the radiative forcing induced by the GSLA increase and 64.9% of that induced by surface albedo variations in non-barren, non-conversion regions. Specifically, the increase in PV greenness in the Northern Hemisphere resulted in a global land surface mean albedo decrease, which was offset by a decrease in greenness in the Southern Hemisphere (both around 0.00093 in magnitude; Fig. 6a and Extended Data Fig. 8a). Globally, the recent changes in PV explained 6.1% of the global mean radiative forcing induced by the GSLA change (Fig. 6a and Extended Data Fig. 9a). Increases in NPV led to a global land surface mean albedo increase by 0.0014, contributing to 43.6% of GSLA change (Fig. 6a and Extended Data Fig. 8b) and 33.7% to the GSLA-induced negative radiative forcing. Furthermore, the change in SWC worldwide raised the global land surface mean albedo by 0.0003 (Fig. 6a and Extended Data Fig. 8c), contributing to 10.0% of the GSLA-induced negative forcing (Extended Data Fig. 9b,c).

In recent decades, widespread greening was observed across most regions globally[35–37]. Vegetation greening could reduce surface albedo because plants absorbed more solar energy for photosynthesis[38–40]. However, some of the increases in PV were converted to NPV in winter, leading to an albedo increase[41]. This albedo enhancement effect was particularly strong in January and February (Extended Data Fig. 10)[42]. The response of albedo to changes in PV and NPV changes varied with LULC types and spatial locations. Albedo in regions with low normalized difference vegetation index (NDVI) was highly sensitive to PV changes[39,40] with PV changes contributing more to albedo variations than NPV changes (Fig. 6b and Supplementary Fig. 24). For instance, in regions with reduced greenness of shrubs and grasslands in Australia, southern Africa and southern South America, there were substantial increases in albedo. Conversely, in regions with increased greenness in shrublands, such as the southwestern United States and the Indian Peninsula, albedo decreased[43,44]. In regions with high NDVI values, the sensitivity of PV-associated albedo to NDVI growth decreased. There was more vegetation browning in high-density vegetation types in winter[44], and thus the changes in NPV often contributed more to albedo than those of PV (Fig. 6b and Supplementary Fig. 24). As a result, despite broader greening trends, many of the greening regions in the Northern Hemisphere still experienced albedo increases.

In the four LULC classification schemes, albedo increases in shrublands were primarily driven by the PV change. For short natural vegetation types (natural herbaceous, grasslands and savannas) and cropland, NPV played a dominant role in the albedo increase (Supplementary Fig. 25). For instance, under LCCS 2, the PV explained 62.3% of the albedo change of shrublands. NPV explained 86.7 and 176.3% of the albedo changes over natural herbaceous and herbaceous croplands, respectively (Supplementary Fig. 25b).

Discussion

Understanding the magnitude and causes of the global land surface albedo change is essential to benchmark the pace of climate change. Our study demonstrates the importance of global land surface mean albedo changes for climate forcing. Albedo in snow-free regions experience a substantial increase (2.2%, 0.0038 (0.0036, 0.0039)), leading to a 0.72% global land surface mean albedo increase (0.0018 (0.0006, 0.0029)). The albedo increase in snow-free regions results in

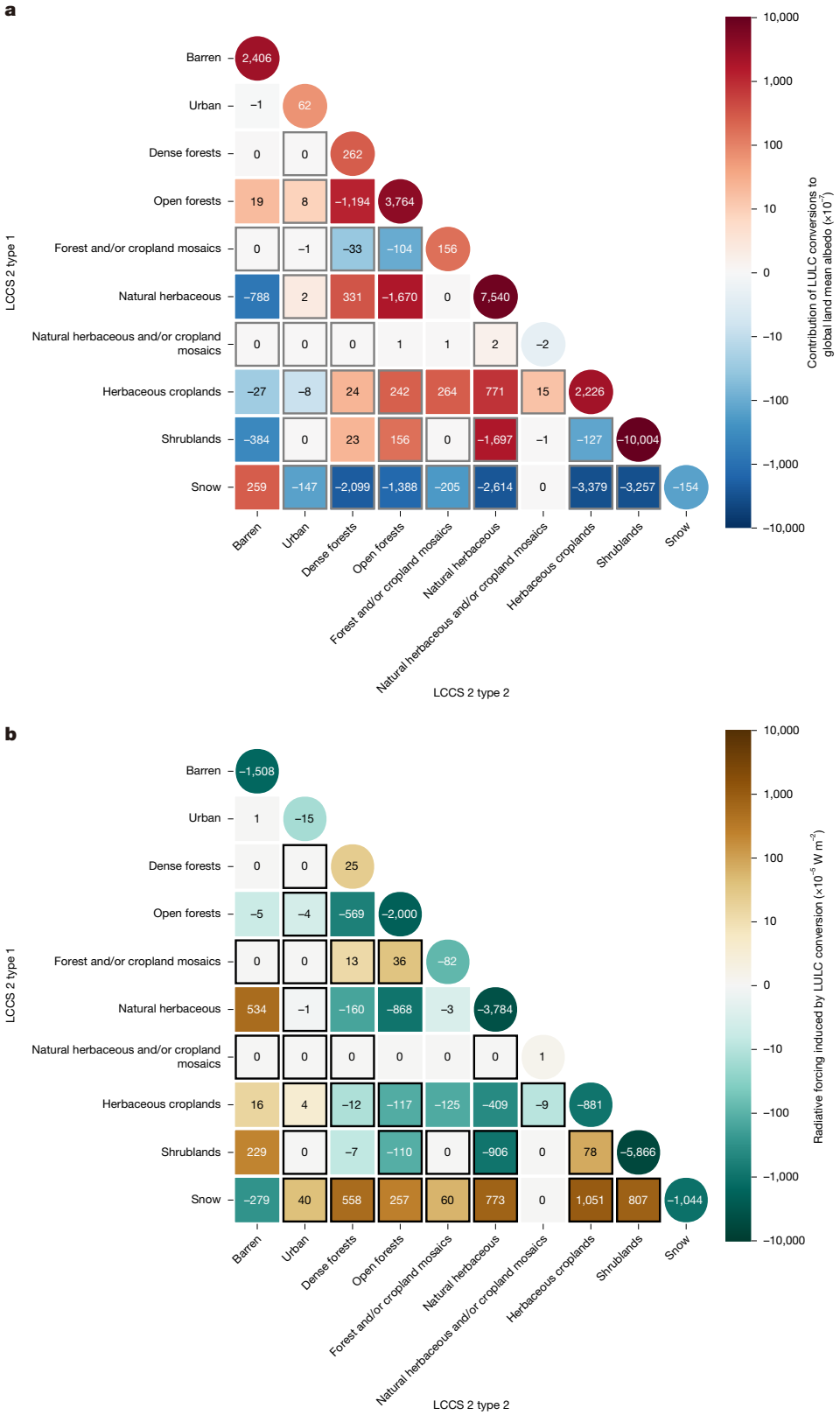

Fig. 5 | Global land surface mean albedo change and global mean radiative forcing resulting from each net bidirectional LULC conversion and each LULC non-conversion region defined by LCCS 2. a, Global land surface mean albedo change. For each square or circle, the colour and the number inside represent the magnitude of the global land surface mean albedo increase. The black outline denotes net conversions from LULC type 1 to type 2; otherwise, it indicates net conversions from type 2 to type 1. Circles denote contributions from LULC non-conversion regions. **b**, As for **a** but for albedo-induced global mean radiative forcing. For each square or circle, the colour and the number inside represent the magnitude of radiative forcing.

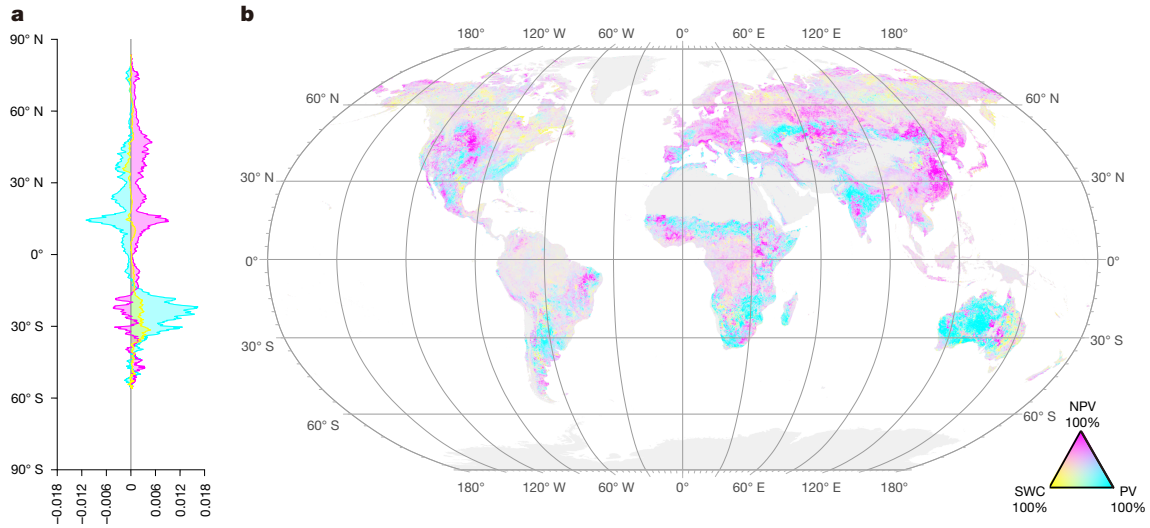

Fig. 6 | Contributions of PV, NPV and SWC to the land surface albedo change in the LULC non-conversion regions. a, Average albedo changes at different latitudes associated with PV, NPV and SWC. **b**, Marginal contribution of PV, NPV and SWC to the land surface albedo change over non-barren, non-conversion regions defined by LCCS 2. Areas are colour-coded according to the component that contributes the most to albedo changes during 2001–2020. The areal fraction in each pixel is calculated within a spatial moving window covering the surrounding 10-km range.

considerable negative global mean radiative forcing (−0.164 (−0.186, −0.138) W m^{-2}), equivalent in magnitude to 59.9% of CO_2 radiative forcing and 48.9% of total greenhouse gas emissions radiative forcing during the period 2011–2019, as reported by the IPCC AR6 (ref. 10). Globally, snow change results in a 0.0013 decrease in global land surface mean albedo, but the induced radiative forcing accounted for only −13.5% (0.0222 (0.0105, 0.0280) W m^{-2}) of the radiative forcing due to the GSLA increase. LULC conversions only contribute to 12.6–20.1% of the GSLA increase under the four LULC classification schemes. The negative global mean radiative forcing originating from LULC conversion (0.0178–0.0333 W m^{-2}) is only 12.3% (IGBP) to 25.3% (LCCS 1) of the forcing from LULC non-conversion regions.

The increase in GSLA is mainly attributed to LULC non-conversion regions (77.9–87.4%). In these regions, shrublands and short natural vegetation types have the largest effects on global land surface mean albedo and radiative forcing among all of the non-snow LULC types in different LULC classification schemes. Albedo varies greatly across different LULC types. Even the same LULC types can play different roles in albedo change in different regions. These spatial differences are be related to different levels of greenness. The decreases in PV in Southern Hemisphere LULC non-conversion regions, coupled with the increase in NPV in the Northern Hemisphere regions, are the primary drivers of GSLA increase.

There are some limitations in this study, including the disregard for anisotropic scattering of diffuse skylight and the use of high-uncertainty albedo data to calculate radiative forcing in regions with solar zenith angles up to 70°–85°. For more details on the limitations and their potential effects, please refer to Supplementary Text 6.

The Earth energy budget variations due to surface albedo changes and trends may profoundly affect local-to-global climate, and their influence may be further complicated with different biophysical processes in near future. Thus, global land surface albedo changes need to be considered in future climate change assessments, especially over regions experiencing long-term changes in vegetation and SWC. Our findings improve the understanding of biophysical feedback mechanisms related to surface albedo, and can inform land management policies aimed at climate mitigation by accounting for the climate effects of albedo change. Our observation-driven methodology provides a baseline for developing monitoring and verification guidelines for land-based climate change mitigation efforts.

Online content

Any methods, additional references, Nature Portfolio reporting summaries, source data, extended data, supplementary information, acknowledgements, peer review information; details of author contributions and competing interests; and statements of data and code availability are available at https://doi.org/10.1038/s41586-025-08987-z.

1. Turner, B. L., Lambin, E. F. & Reenberg, A. The emergence of land change science for global environmental change and sustainability. *Proc. Natl Acad. Sci. USA* **104**, 20666–20671 (2007).
2. Pongratz, J., Reick, C. H., Raddatz, T. & Claussen, M. Biogeophysical versus biogeochemical climate response to historical anthropogenic land cover change. *Geophys. Res. Lett.* **37**, L08702 (2010).
3. Forzieri, G., Alkama, R., Miralles, D. G. & Cescatti, A. Satellites reveal contrasting responses of regional climate to the widespread greening of Earth. *Science* **356**, 1180–1184 (2017).
4. Ouyang, Z. et al. Albedo changes caused by future urbanization contribute to global warming. *Nat. Commun.* **13**, 3800 (2022).
5. Sherwood, S. C., Dixit, V. & Salomez, C. The global warming potential of near-surface emitted water vapour. *Environ. Res. Lett.* **13**, 104006 (2018).
6. Andrews, T., Betts, R. A., Booth, B. B. B., Jones, C. D. & Jones, G. S. Effective radiative forcing from historical land use change. *Clim. Dyn.* **48**, 3489–3505 (2017).
7. Lejeune, Q. et al. Biases in the albedo sensitivity to deforestation in CMIP5 models and their impacts on the associated historical radiative forcing. *Earth Syst. Dyn.* **11**, 1209–1232 (2020).
8. Ghimire, B. et al. Global albedo change and radiative cooling from anthropogenic land cover change, 1700 to 2005 based on MODIS, land use harmonization, radiative kernels, and reanalysis. *Geophys. Res. Lett.* **41**, 9087–9096 (2014).
9. Hasler, N. et al. Accounting for albedo change to identify climate-positive tree cover restoration. *Nat. Commun.* **15**, 2275 (2024).
10. IPCC *Climate Change 2021: The Physical Science Basis* (eds Masson-Delmotte, V. et al.) (Cambridge Univ. Press, 2021).
11. Bala, G. et al. Combined climate and carbon-cycle effects of large-scale deforestation. *Proc. Natl Acad. Sci. USA* **104**, 6550–6555 (2007).
12. Betts, R. A., Falloon, P. D., Goldewijk, K. K. & Ramankutty, N. Biogeophysical effects of land use on climate: model simulations of radiative forcing and large-scale temperature change. *Agric. For. Meteorol.* **142**, 216–233 (2007).
13. Bonan, G. B. Forests and climate change: forcings, feedbacks, and the climate benefits of forests. *Science* **320**, 1444–1449 (2008).
14. Bright, R. M., Zhao, K., Jackson, R. B. & Cherubini, F. Quantifying surface albedo and other direct biogeophysical climate forcings of forestry activities. *Glob. Change Biol.* **21**, 3246–3266 (2015).
15. Weber, J. et al. Chemistry-albedo feedbacks offset up to a third of forestation's CO2 removal benefits. *Science* **383**, 860–864 (2024).
16. Duveiller, G., Hooker, J. & Cescatti, A. The mark of vegetation change on earth's surface energy balance. *Nat. Commun.* **9**, 679 (2018).
17. Anderson, R. G. et al. Biophysical considerations in forestry for climate protection. *Front. Ecol. Environ.* **9**, 174–182 (2011).
18. Schaaf, C. Z. W. MODIS/terra+aqua BRDF/albedo daily L3 Global—500 m V061. *NASA Earth Data* https://doi.org/10.5067/MODIS/MCD43A3.061 (2021).

19. Dumont, M. et al. Contribution of light-absorbing impurities in snow to Greenland's darkening since 2009. *Nat. Geosci.* **7**, 509–512 (2014).
20. Xu, X., Huang, A., Belle, E., De Frenne, P. & Jia, G. Protected areas provide thermal buffer against climate change. *Sci. Adv.* **8**, 0119 (2022).
21. Venter, Z. S., Chakraborty, T. & Lee, X. Crowdsourced air temperatures contrast satellite measures of the urban heat island and its mechanisms. *Sci. Adv.* **7**, 9569 (2021).
22. Guirado, E. et al. The global biogeography and environmental drivers of fairy circles. *Proc. Natl Acad. Sci. USA* **120**, 2304032120 (2023).
23. Jääskeläinen, E., Manninen, T., Hakkarainen, J. & Tamminen, J. Filling gaps of black-sky surface albedo of the Arctic sea ice using gradient boosting and brightness temperature data. *Int. J. Appl. Earth Observ. Geoinf.* **107**, 102701 (2022).
24. Zemp, D. C. et al. Self-amplified Amazon forest loss due to vegetation-atmosphere feedbacks. *Nat. Commun.* **8**, 14681 (2017).
25. Liu, N. F. et al. A statistics-based temporal filter algorithm to map spatiotemporally continuous shortwave albedo from MODIS data. *Hydrol. Earth Syst. Sci.* **17**, 2121–2129 (2013).
26. Hall, D. K., Salomonson, V. V. & Riggs, G. A. MODIS/terra snow cover daily L3 global 500 m grid. Version 6. *NSIDC* https://nsidc.org/data/mod10a1/versions/61 (2016).
27. Friedl, M. & Sulla-Menashe., D. MODIS/terra+aqua land cover type yearly L3 global 500m SIN grid V061. *NASA Earth Data* https://doi.org/10.5067/MODIS/MCD12Q1.061 (2022).
28. Casey, K. A., Polashenski, C. M., Chen, J. & Tedesco, M. Impact of MODIS sensor calibration updates on Greenland Ice Sheet surface reflectance and albedo trends. *Cryosphere* **11**, 1781–1795 (2017).
29. Di Gregorio, A. *Land Cover Classification System: Classification Concepts and User Manual Softwave V2* (Food and Agriculture Organization of the United Nations (FAO), 2005).
30. Di Gregorio, A. & Jansen, L. J. M. A new concept for a land-cover classification system. *Land* **2**, 55–65 (1998).
31. Loveland, T. R. & Belward, A. S. The igbp-dis global 1km land cover data set, discover: first results. *Int. J. Remote Sens.* **18**, 3289–3295 (1997).
32. Sulla-Menashe, D., Gray, J. M., Abercrombie, S. P. & Friedl, M. A. Hierarchical mapping of annual global land cover 2001 to present: the MODIS collection 6 land cover product. *Remote Sens. Environ.* **222**, 183–194 (2019).
33. Tian, J. et al. Simultaneous estimation of fractional cover of photosynthetic and non-photosynthetic vegetation using visible-near infrared satellite imagery. *Remote Sens. Environ.* **290**, 113549 (2023).
34. Wang, L. & Qu, J. J. NMDI: a normalized multi-band drought index for monitoring soil and vegetation moisture with satellite remote sensing. *Geophys. Res. Lett.* **34**, L20405 (2007).
35. Zhu, Z. et al. Greening of the Earth and its drivers. *Nat. Clim. Change* **6**, 791–795 (2016).
36. Cui, J. et al. Global water availability boosted by vegetation-driven changes in atmospheric moisture transport. *Nat. Geosci.* **15**, 982–988 (2022).
37. Chen, C. et al. China and India lead in greening of the world through land-use management. *Nat. Sustain.* **2**, 122–129 (2019).
38. Peng, S. et al. Multi-staged NDVI dependent snow-free land-surface shortwave albedo narrowband-to-broadband (NTB) coefficients and their sensitivity analysis. *Remote Sens.* **9**, 93 (2017).
39. Ma, Z., Xie, Y., Jiao, J., li, L. & Wang, X. The construction and application of an albedo-NDVI based desertification monitoring model. *Procedia Environ. Sci.* **10**, 2029–2035 (2011).
40. Pang, G., Chen, D., Wang, X. & Lai, H.-W. Spatiotemporal variations of land surface albedo and associated influencing factors on the Tibetan Plateau. *Sci. Total Environ.* **804**, 150100 (2022).
41. Newnham, G. J., Verbesselt, J., Grant, I. F. & Anderson, S. A. J. Relative Greenness Index for assessing curing of grassland fuel. *Remote Sens. Environ.* **115**, 1456–1463 (2011).
42. Guerschman, J. P. et al. Estimating fractional cover of photosynthetic vegetation, non-photosynthetic vegetation and bare soil in the Australian tropical savanna region upscaling the EO-1 Hyperion and MODIS sensors. *Remote Sens. Environ.* **113**, 928–945 (2009).
43. Piao, S. et al. Characteristics, drivers and feedbacks of global greening. *Nat. Rev. Earth Environ.* **1**, 14–27 (2020).
44. Qiu, B. et al. Dense canopies browning overshadowed by global greening dominant in sparse canopies. *Sci. Total Environ.* **826**, 154222 (2022).

Methods

To reconstruct land surface albedo, explore its temporal evolution and explain the underlying key mechanisms, we implement a series of data-driven analyses that are detailed in the following sections and summarized in the scheme shown in Extended Data Fig. 1.

ALLUMs

We construct a total of four ALLUM datasets including ALLUM-LCCS 1, ALLUM-LCCS 2, ALLUM-LCCS 3 and ALLUM-IGBP, each of which is based on different LULC classification schemes. Each ALLUM is a multi-dimensional array in which the monthly global land surface albedo and conversions among 9–16 LULC types corresponding to a specific classification scheme are stored in 1° × 1° grid cells from 2001 to 2020. Specifically, each grid cell contains for each monthly time step: (1) the values of terrestrial white- and black-sky albedo in shortwave (0.3–5.0 μm), visible light (0.3–0.7 μm) and near-infrared (0.7–5.0 μm) bands for the total of 50 LULC types with respect to the four LULC classification schemes (Supplementary Tables 1–3); (2) the areal extent of each LULC type and (3) the areas of LULC changes in each month from 2002 to 2020 relative to the same month in 2001 across 612 LULC conversion pathways, and the areas of LULC non-conversion regions for 50 LULC types under the four LULC classification schemes. The ALLUMs exclude the regions with solar zenith angles greater than 85°, where there is negligible downward radiation at the land surface. The reconstruction involves aggregating 500-m-resolution monthly snow fraction, yearly LULC and monthly albedo data to 1° × 1° grid cells. Details on the aggregation methods are reported in the following paragraphs.

Snow fraction. On the basis of daily 500-m-resolution snow cover fraction (SCF) data acquired from the MOD10A1 C6.1 (ref. 26), we synthesize a global monthly snow cover product. SCF is given as a percentage per pixel. The following three sequential steps are used to fill in missing values caused by cloud cover and/or limited coverage of observations at the monthly scale and to generate gap-free monthly SCF.

1. Missing daily data are initially reconstructed using the values from the temporally nearest data within the previous 8-day cycle[45].
2. The monthly SCF data are synthesized using the mean compositing method from the daily data.
3. The remaining missing data, originating from consecutive or systematic missing retrievals that cannot be reconstructed by steps (1) and (2), are interpolated using the IDW interpolation model[46].

LULC map. The MCD12Q1 C6.1 product provides several different classification layers of land cover types from 2001 to 2020 at 500-m resolution[27]. We use the IGBP classification scheme and the LCCS 1–3 classification schemes to generate four ALLUMs, which separately define 16, 15, 10 and 9 LULC types excluding water bodies. Owing to large seasonal variations in snow cover, snow is taken in each of ALLUMs as a separate land cover class and merged with the permanent snow class, through setting an empty LULC type and 100% SCF in permanent snow region defined by the corresponding LULC scheme. The snow type is represented by the SCF rather than a discrete classification value. Each pixel in the grid cells includes the attributes of annual LULC types and monthly SCFs. This indicates that the land areas with different LULC types may change on a monthly scale due to variations in snow cover.

Surface albedo. Surface albedo values are retrieved from the MCD43A3 C6.1 albedo dataset[18]. The product provides daily directional hemispherical reflectance (black-sky albedo) and bihemispherical reflectance (white-sky albedo) for three broad spectrum bands (shortwave 0.3–5.0 μm, visible light 0.3–0.7 μm and near-infrared 0.7–5.0 μm) at 500-m-resolution. Each daily image is generated using the data from a 16-day period centred on the given day. To synthesize monthly average snow and snow-free albedo of white and black sky for each band, we distinguish between snow albedo and snow-free albedo pixels. We exploit the daily snow albedo mask derived from MCD43A2 C6.1 (ref. 47) to achieve this. Because the MCD43 albedo algorithm is not validated for water bodies, we mask water albedo data defined by the LULC maps.

Area, white- and black-sky albedo of each LULC type. In each of the four ALLUMs, the snow cover area $A^{\mathrm{snow}}(y, m, \mathrm{lon}, \mathrm{lat})$ in a 1° × 1° grid cell, located at latitude (lat) and longitude (lon) is the sum of the snow areas from all 500-m-resolution pixels, in month m and year y. For other LULC types, $A^{t}(y, m, \mathrm{lon}, \mathrm{lat})$ is the sum of the snow-free areas for pixels belonging to a specific LULC type t. The snow and snow-free areas for each pixel are separately calculated by multiplying the pixel area with SCF and (1 − SCF).

In each 1° × 1° grid cell, albedo of snow is the albedo average in all snow pixels. Similarly, albedo of each of non-snow LULC types is the average of all albedo in the snow-free pixels belonging to that LULC type. Missing albedo values are reconstructed using the four-dimensional IDW interpolation model in combination with data anisotropies based on several nearby known albedo values with the same LULC type, spectral band and albedo type (white or black sky). Details on the four-dimensional IDW interpolation are reported in Supplementary Text 1.

Areas of LULC conversions. On the basis of the monthly LULC data resulting from annual LULC information and the monthly variations in snow cover, we compute the LULC type conversion areas ($\mathrm{LCA}_{\mathrm{pixel}}$) between two time periods time0 and time1 in each 500-m-resolution pixel where non-snow LULC type $t1$ and $\mathrm{SCF}_{\mathrm{time0}}$ are converted to non-snow LULC type $t2$ and $\mathrm{SCF}_{\mathrm{time1}}$, where time0 and time1 represent any month in 2001 and the same month in a specific year between 2002 and 2020, respectively. The computation takes into account variations in land cover types and snow cover and is based on the following two principles as shown in Supplementary Fig. 26: (1) the sum of the areas of persistent snow cover regions ($\mathrm{LCA}_{\mathrm{pixel}}^{\mathrm{snow}\to\mathrm{snow}}$), the areas of changed snow cover regions ($\mathrm{LCA}_{\mathrm{pixel}}^{\mathrm{snow}\to t2}$ and $\mathrm{LCA}_{\mathrm{pixel}}^{t1\to\mathrm{snow}}$) and the areas of snow-free regions with conversion among other LULC types ($\mathrm{LCA}_{\mathrm{pixel}}^{t1\to t2}$) equals the total area of the pixel A_{pixel}; (2) the area of snow-covered regions equals $\mathrm{LCA}_{\mathrm{pixel}}^{\mathrm{snow}\to\mathrm{snow}}$ in the period with less snow cover; the area of snow-free regions equals $\mathrm{LCA}_{\mathrm{pixel}}^{t1\to t2}$ in the period with more snow cover.

To this aim, we first obtain the area of persistent snow cover ($\mathrm{LCA}_{\mathrm{pixel}}^{\mathrm{snow}\to\mathrm{snow}}$) and the area of the conversion from $t1$ to $t2$ ($\mathrm{LCA}_{\mathrm{pixel}}^{t1\to t2}$) using equations (1) and (2):

$$\mathrm{LCA}_{\mathrm{pixel}}^{\mathrm{snow}\to\mathrm{snow}} = A_{\mathrm{pixel}} \min(\mathrm{SCF}_{\mathrm{time0}}, \mathrm{SCF}_{\mathrm{time1}}) \quad (1)$$

$$\mathrm{LCA}_{\mathrm{pixel}}^{t1\to t2} = A_{\mathrm{pixel}}(1 - \max(\mathrm{SCF}_{\mathrm{time0}}, \mathrm{SCF}_{\mathrm{time1}})) \quad (2)$$

The area of conversion between snow and $t1$ or $t2$ can then be quantified depending on the changes in snow cover conditions.

If $\mathrm{SCF}_{\mathrm{time0}} > \mathrm{SCF}_{\mathrm{time1}}$, the conversion areas are retrieved as follows:

$$\mathrm{LCA}_{\mathrm{pixel}}^{\mathrm{snow}\to t2} = A_{\mathrm{pixel}}(\max(\mathrm{SCF}_{\mathrm{time0}}, \mathrm{SCF}_{\mathrm{time1}}) - \min(\mathrm{SCF}_{\mathrm{time0}}, \mathrm{SCF}_{\mathrm{time1}})) \quad (3)$$

$$\mathrm{LCA}_{\mathrm{pixel}}^{t1\to\mathrm{snow}} = 0 \quad (4)$$

If $\mathrm{SCF}_{\mathrm{time0}} \le \mathrm{SCF}_{\mathrm{time1}}$, the conversion areas are retrieved as follows:

$$\mathrm{LCA}_{\mathrm{pixel}}^{t1\to\mathrm{snow}} = A_{\mathrm{pixel}}(\max(\mathrm{SCF}_{\mathrm{time0}}, \mathrm{SCF}_{\mathrm{time1}}) - \min(\mathrm{SCF}_{\mathrm{time0}}, \mathrm{SCF}_{\mathrm{time1}})) \quad (5)$$

$$\mathrm{LCA}_{\mathrm{pixel}}^{\mathrm{snow}\to t2} = 0 \quad (6)$$

The area of each LULC conversion pathway in a grid cell is the sum of all $\mathrm{LCA}_{\mathrm{pixel}}$ in that grid cell with the same conversion pathways.

Blue-sky albedo

In MCD43A3 C6.1, white- and black-sky albedo represent two conceptual scenarios of albedo under isotropic diffuse conditions and direct illumination, respectively. Blue-sky albedo, which represents the actual surface albedo under natural illumination conditions, is derived from them using the fraction of diffuse downward radiation (DDRF) as the weight factor. We derive DDRF in shortwave lights by exploiting monthly diffuse and direct surface solar radiation fluxes in the visible (vis) and near-infrared (NIR) spectra provided by the National Centers for Environmental Prediction Reanalysis Derived Products for the period 2001–2020[48] based on equation (7)[8,25]:

$$\mathrm{DDRF}(y, m, \mathrm{lon}, \mathrm{lat}, \mathrm{shortwave}) = \frac{\mathrm{DDR}(y, m, \mathrm{lon}, \mathrm{lat}, \mathrm{NIR}) + \mathrm{DDR}(y, m, \mathrm{lon}, \mathrm{lat}, \mathrm{vis})}{\mathrm{BDR}(y, m, \mathrm{lon}, \mathrm{lat}, \mathrm{NIR}) + \mathrm{BDR}(y, m, \mathrm{lon}, \mathrm{lat}, \mathrm{vis}) + \mathrm{DDR}(y, m, \mathrm{lon}, \mathrm{lat}, \mathrm{NIR}) + \mathrm{DDR}(y, m, \mathrm{lon}, \mathrm{lat}, \mathrm{vis})} \quad (7)$$

where BDR and DDR denote the beam downward radiation and the diffuse downward radiation, respectively.

Under the assumption of isotropy in skylight scattering, we calculate blue-sky albedo in the shortwave bands on the basis of DDRF of the corresponding band (equation (8)):

$$\alpha_{\mathrm{blue}} = \alpha_{\mathrm{white}}\mathrm{DDRF} + \alpha_{\mathrm{black}}(1 - \mathrm{DDRF}) \quad (8)$$

Validation of reconstructed global monthly albedo data

Four-dimensional spatio-temporal IDW interpolation. In constructing the ALLUMs, the four-dimensional spatio-temporal IDW interpolation model is used to fill in missing albedo values for the 50 LULC types over the four classification schemes. For the validation purpose, we randomly select 2 million grid-level albedo cells where land surface has no missing albedo values. In these grid cells, white- and black-sky albedo values of different bands for each LULC type serve as ground truth to evaluate the credibility of the interpolated data.

Validation of reconstructed global monthly 500-m-resolution albedo data. We separately use the four ALLUMs to reconstruct global monthly 500-m-resolution shortwave albedo. Specifically, the 500-m-resolution white- or black-sky albedo of a pixel with a LULC type t is calculated by weighting the albedo $\alpha^{t}_{\mathrm{white/black}}(y, m)$ of t and snow albedo $\alpha^{\mathrm{snow}}_{\mathrm{white/black}}(y, m)$ with the SCF of the pixel (equation (9)). The LULC type and SCF of the pixel are determined by the monthly 500-m-resolution LULC and SCF datasets, respectively. $\alpha_{\mathrm{white/black}}$ is retrieved from the ALLUMs in the grid cell where the pixel locates as follows:

$$\alpha_{\mathrm{white/black,pixel}}(y, m) = \alpha^{t}_{\mathrm{white/black}}(y, m)[1 - \mathrm{SCF}(y, m)] + \alpha^{\mathrm{snow}}_{\mathrm{white/black}}(y, m)\mathrm{SCF}(y, m) \quad (9)$$

We then reconstruct the 500-m-resolution blue-sky albedo using equation (8), and compare it to the blue-sky albedo value synthesized from the original MCD43A3 C6.1 black- and white-sky albedo to verify the reliability of the ALLUMs (Extended Data Fig. 1b). We select 4.8 million points from the two blue-sky albedo datasets to validate the accuracy of the reconstructed results. Random sampling with strict buffer[49] is used to avoid biases due to spatial autocorrelation. Each random point is at least 10 km from its nearest neighbours.

Contributions to changes in global land surface mean albedo

Changes in global land surface mean albedo. Satellite albedo retrievals tend to be inaccurate for solar zenith angles exceeding 70° (ref. 50), and this has also been confirmed and supported in the validation of our reconstructed data (Supplementary Fig. 5). Thus, we calculate global land surface mean albedo by using the monthly albedo from the regions with a solar zenith angle less than 70° as follows:

$$\alpha_{\mathrm{GL}}(y) = \frac{1}{A_{\mathrm{GL}}}\sum_{\mathrm{lat}=-90}^{90}\sum_{\mathrm{lon}=-180}^{180}\sum_{t=1}^{N_t}\frac{\sum_{m=1}^{12}\alpha^{t}_{\mathrm{blue}}(y, m, \mathrm{lon}, \mathrm{lat})A^{t}(y, m, \mathrm{lon}, \mathrm{lat})M_{70}(y, m, \mathrm{lon}, \mathrm{lat})T_{\mathrm{m}}(m)}{\sum_{m=1}^{12}M_{70}(y, m, \mathrm{lon}, \mathrm{lat})T_{\mathrm{m}}(m)} \quad (10)$$

where A_{GL} is the global land area (147.9 million km^2). N_t is the number of LULC types in each of the four LULC classification schemes. $M_{70} = 0$ if the maximum solar zenith angle of the day is greater than 70°; otherwise, $M_{70} = 1$. T_{m} denotes 1 month with units of seconds in a normal year. We neglect the difference of the month length between normal years and leap years. These calculations are performed separately for each ALLUM dataset specific to different classification schemes.

Contributions of LULC and snow dynamics. In the conversion from $t1$ to $t2$, there are N_{t}^2 pathways for N_{t} LULC types in each 1° × 1° grid cell. $(N_{\mathrm{t}}-1)^2 - (N_{\mathrm{t}}-1)$ pathways ($t1 \neq t2$ and both $t1$ and $t2$ are not snow) represent the global land surface mean albedo change due to LULC conversions in snow-free regions. The contribution of snow dynamics is contained within the $N_{\mathrm{t}}^2 - (N_{\mathrm{t}}-1)^2$ snow-related pathways ($t1$ = snow or $t2$ = snow).

On the basis of the areas of the LULC conversions through each of the pathways in each 1° × 1° grid cell, $\mathrm{LCA}^{t1\to t2}(y, m, \mathrm{lon}, \mathrm{lat})$ and the blue-sky shortwave albedo for different LULC types and time $\alpha^{t}_{\mathrm{blue}}(y, m, \mathrm{lon}, \mathrm{lat})$, we compute the global land surface mean albedo change caused by the conversion between any two LULC types $C_{a\mathrm{GL}}(y)$ by using equations (11) and (12), with the year 2001 as the reference:

$$C^{t1\to t2}_{a\mathrm{GL}}(y) = \frac{1}{A_{\mathrm{GL}}}\sum_{\mathrm{lat}=-90}^{90}\sum_{\mathrm{lon}=-180}^{180}\frac{\sum_{m=1}^{12}\Delta\alpha^{t1\to t2}_{\mathrm{blue}}(y, m, \mathrm{lon}, \mathrm{lat})\mathrm{LCA}^{t1\to t2}(y, m, \mathrm{lon}, \mathrm{lat})M_{70}(y, m, \mathrm{lon}, \mathrm{lat})T_{\mathrm{m}}(m)}{\sum_{m=1}^{12}M_{70}(y, m, \mathrm{lon}, \mathrm{lat})T_{\mathrm{m}}(m)} \quad (11)$$

$$\Delta\alpha^{t1\to t2}_{\mathrm{blue}}(y, m, \mathrm{lon}, \mathrm{lat}) = \alpha^{t2}_{\mathrm{blue}}(y, m, \mathrm{lon}, \mathrm{lat}) - \alpha^{t1}_{\mathrm{blue}}(2001, m, \mathrm{lon}, \mathrm{lat}) \quad (12)$$

where y spans the 2002–2020 period.

The contribution of GSLA to global land surface mean albedo change $C^{\mathrm{GSLA}}_{a\mathrm{GL}}(y)$ is $\sum_{t1}^{t1\neq\mathrm{snow}}\sum_{t2}^{t2\neq\mathrm{snow}}C^{t1\to t2}_{a\mathrm{GL}}(y)$. Then the relative contribution of each LULC conversion to the GSLA change is quantified as a percentage value, by dividing $C^{t1\to t2}_{a\mathrm{GL}}(y)$ by $C^{\mathrm{GSLA}}_{a\mathrm{GL}}(y)$ and multiplying by 100%.

Contributions of LULC non-conversion regions. For the LULC non-conversion regions, there are $N_{\mathrm{t}} - 1$ pathways ($t1 = t2$, and both $t1$ and $t2$ are not snow) representing the global land surface mean albedo change owning to changes in land attributes in snow-free regions (LULC non-conversions), such as an increase in forest density. The contribution of each LULC non-conversion pathway is calculated using the same method (equations (11) and (12)) as other pathways.

To explain the reasons for albedo changes in non-conversion regions, a multivariate linear regression model (equation (13)) is used to fit monthly shortwave albedo changes in each pixel from MCD43A3 C6.1 (Extended Data Fig. 1c):

$$\alpha_{\mathrm{pixel}} = \frac{\partial\alpha_{\mathrm{pixel}}}{\partial\ln\mathrm{NDVI}}\ln\mathrm{NDVI} + \frac{\partial\alpha_{\mathrm{pixel}}}{\partial\mathrm{SSI}}\mathrm{SSI} + \frac{\partial\alpha_{\mathrm{pixel}}}{\partial\mathrm{NMDI}}\mathrm{NMDI} + \varepsilon \quad (13)$$

where ε represents the model residuals, NDVI[51] was defined in the main text, and SSI and NMDI denote the spectral shape index[33] and the normalized multi-band drought index[34], respectively. NDVI, SSI and NMDI are used to characterize the PV cover, NPV cover and SWC, respectively. NDVI is transformed by using the natural logarithm in the

regression model to account for the nonlinear relationship between NDVI and albedo[52].

The multivariate linear regression model described in equation (13) is chosen because it represents a simple and reasonable approach to capture possible emerging first-order temporal changes in the signal that can be applied consistently on the long time series data and across different products and variables. The NDVI, SSI and NMDI from 2001 to 2020 are taken from the MOD09A1 C6.1 (ref. 53) 500-m-resolution 8-daily surface reflectance dataset. Their calculation methods are detailed in Supplementary Table 5. NDVI, SSI and NMDI data are composited into monthly data by taking the mean of 8-day retrievals, after masking out snow and clouds conditions retrieved from the product quality bands. The albedo data fitted in equation (13) is monthly averaged white- and black-sky snow-free albedo synthesized from MCD43A3 C6.1 for each pixel from 2001 to 2020.

The model (equation (13)) is applied to each month m, 500-m-resolution pixel p and albedo type w (white or black sky) to individually regress the albedo sensitivity of the three components $\frac{\partial \alpha_{\text{pixel}}}{\partial Z}(m,p,w)$ (Z represent lnNDVI, SSI or NMDI). In the regions with solar zenith angles less than 85°, r^2 of the model for predicting white- and black-sky albedo are 0.93 and 0.94, respectively, with r.m.s.e. values of 0.010 and 0.009 (Supplementary Fig. 23). These results indicate that the model can estimate the albedo accurately. The contribution of these three components to the albedo changes for each month and 500-m-resolution pixel is estimated by using equation (14):

$$C^{Z}_{\alpha-\text{pixel}}(m,p,w) = \frac{\partial \alpha_{\text{pixel}}}{\partial Z}(m,p,w)\Delta Z(m,p) \\ (1-\max(\text{SCF}_{2001}(m,p), \text{SCF}_{2020}(m,p)) \quad (14)$$

where ΔZ is the difference in Z between 2020 and 2001.

The three components-induced global land surface mean albedo change is calculated by weighting and summing $C^{Z}_{\alpha-\text{pixel}}(m,p,w)$. For details, please refer to Supplementary Text 7.

Albedo-induced radiative forcing

To estimate the top of the atmosphere radiative forcing induced by the land surface albedo changes, we use six grid-cell specific all-sky albedo radiative kernels, which are resampled to align with the 1° × 1° ALLUM grid cells using the bilinear interpolation. These kernels represent the change of net shortwave radiation flux at the top of the atmosphere in response to a 0.01 change of surface albedo. These six kernels are generated on the basis of four models, CAM5 (ref. 54), HadGEM2 (ref. 55), HadGEM3 (ref. 56) and ECHAM6 (ref. 57) and two reanalysis datasets, including ERAI[58] and ERA5 (ref. 59).

Using the ALLUMs and six shortwave radiative kernel datasets, we calculate the yearly global mean radiative forcing $\text{GMRF}^{t1\to t2}(y)$ induced by the conversion between any two LULC types (equation (15)). We finally take the maximum and minimum values of the radiative forcing calculated by different radiative kernels as the uncertainty range:

$$\text{GMRF}^{t1\to t2}(y) = \frac{100}{A_{\text{global}}T_{\text{y}}}\sum_{\text{lat}=-90}^{90}\sum_{\text{lon}=-180}^{180}\sum_{m=1}^{12} \\ [\Delta\alpha^{t1\to t2}_{\text{blue}}(y,m,\text{lon},\text{lat})\text{LCA}^{t1\to t2}(y,m,\text{lon},\text{lat}) \\ K_{\text{r}}(m,\text{lon},\text{lat})M_{85}(m,\text{lon},\text{lat})T_{\text{m}}(m)] \quad (15)$$

where $K_{\text{r}}(m,\text{lon},\text{lat})$ denotes the shortwave radiation kernel (W m^{-2}) for each month and grid cell, $\Delta\alpha^{t1\to t2}_{\text{blue}}$ is the change in blue-sky shortwave albedo, A_{global} is the global surface area (510 million km^2) and T_{y} denotes one normal year with units of seconds. $M_{85}=0$ if the maximum solar zenith angle of the day is greater than 85°; otherwise, $M_{85}=1$. The value of 100 is used to account for the kernel definition for every 0.01 change in surface albedo. The global mean radiative forcing induced by PV cover, NPV cover and SWC changes is calculated by using the method similar to equation (15). For details, please refer to Supplementary Text 7.

This analysis includes the regions with solar zenith angles up to 85°, which is a broader range than that used to calculate global land surface mean albedo (solar zenith angles less than 70°). This is because the calculation of global mean radiative forcing requires considering the contribution of radiative flux change over the entire land surface, including the regions with solar zenith angles of 70°–85°.

The total albedo-induced radiative forcing is the sum of the GMRF caused by LULC conversions through individual pathways and the albedo change in LULC non-conversion regions (equation (16)):

$$\text{GMRF}_{\text{total}}(y) = \sum_{t1=1}^{N_{\text{t}}}\sum_{t2=1}^{N_{\text{t}}}\text{GMRF}^{t1\to t2}(y) \quad (16)$$

Albedo-induced integrated radiative forcing is the integration of radiative forcing over time and regions. We calculate the integrated radiative forcing caused by the global land surface mean albedo change from 2001 to 2020 (using the year 2001 as the reference), using equation (17), to measure the long-term impact on the overall energy balance of the Earth:

$$\text{RF}_{\text{Integrated}} = A_{\text{global}}T_{\text{y}}\sum_{y=2002}^{2020}\text{GMRF}_{\text{total}}(y) \quad (17)$$

where $\text{RF}_{\text{Integrated}}$ represents the contribution of the albedo change to the shortwave radiation energy variation. A positive radiative forcing value shows that more energy is absorbed at the top of the atmosphere, leading to a net energy gain and contributing to global warming. Conversely, a negative value indicates less energy is absorbed by the Earth.

Uncertainty and sensitivity analysis

To assess the impact of the calibration errors of MODIS sensors, we derive the long-term trends of monthly blue-sky albedo trends at the six pseudo-invariant calibration sites (PICSs) from 2001 to 2020 (Supplementary Fig. 13). The average trend error across the six PICSs is 0.09% per decade. We mask out all the albedo changes below the calibration limit (0.7% per decade on the basis of the largest blue-sky albedo trend in the six PICSs) over the LULC conversion pathways or non-conversion regions in each grid cell in the four ALLUM datasets, and the difference in global land surface mean albedo change was less than 2×10^{-4} before and after the mask in the four ALLUMs, whereas the difference in GSLA was less than 8×10^{-5}. These small differences indicate that the global land surface mean albedo change is little affected by the calibration error. For details, please refer to Supplementary Text 4, Extended Data Fig. 4 and Supplementary Fig. 14. Furthermore, we investigate the regions with albedo trends below the calibration limit in Supplementary Fig. 15 (mainly in Greenland and the Antarctic Ice Sheet), emphasizing the uncertainties associated with these local changes[28].

To further evaluate our results, we calculate the global land surface mean albedo change from 2001 to 2020 using the GLASS02B03 V50 albedo data[60] with an 8-day temporal resolution. The comparison with our ALLUM-based results demonstrates a high consistency in temporal and spatial patterns. Furthermore, we validate the reliability of our results of albedo changes in Greenland and Antarctica by using MOD10A1 C6.1 snow albedo data[26] and long-term automatic weather stations albedo observations[61] (Supplementary Text 3, Extended Data Fig. 3 and Supplementary Figs. 6–11).

We demonstrate here that the impact of LULC misclassification on the albedo accuracy of ALLUMs is negligible. We validate each of the four ALLUMs by using 2 million albedo samples at the grid level and 4.8 million 500-m-resolution samples reconstructed using ALLUMs (section 'Validation of reconstructed global monthly albedo data'). The classification accuracies of the four ALLUMs corresponding to different LULC schemes are very different, that is, the overall classification accuracy of 72, 81 and 87% for LCCS 1–3, respectively, and 67% for IGBP[32]. Yet, albedo accuracy of each of the four ALLUMs shows little

differences (Supplementary Figs. 1–3). Furthermore, the global land and snow-free land surface mean albedo changes from 2001 to 2020 by using ALLUM-LCCS 1–3 and ALLUM-IGBP show very small deviations (less than 0.0003; Supplementary Fig. 12). We calculate the albedo change across four seasons per year by using the four ALLUMs, and use their maximum and minimum values as a measure of the uncertainty introduced to the land surface albedo change.

We use six different radiative kernels to reduce the uncertainty in radiative forcing calculations. The radiative forcing across the six kernels show a high consistency (Figs. 2a and 4b). Although the albedo radiative forcing induced by snow dynamics shows considerable variabilities, it accounts for a very small fraction of the total radiative forcing (Figs. 2a and 4b). We take the maximum and minimum values of radiative forcing using these kernels and the four ALLUMs as the uncertainty range of radiative forcing.

We use the one-sample *t*-test to analyse the statistical significance of change in the global land surface mean albedo, GSLA and the induced radiative forcing, and Mann–Kendall test to examine their trends (Figs. 1a and 2a). We further conduct significance tests within each 3° × 3° grid cell by using the two-sided Student's *t*-test for albedo changes and radiative forcing between two periods (2011–2020 and 2001–2010), and using the Mann–Kendall test for trends over the past two decades. The albedo changes and induced radiative forcing (Figs. 1c and 2c, Extended Data Fig. 2a and Supplementary Fig. 14), as well as their trends (Figs. 1b and 2b, Extended Data Fig. 2b and Supplementary Figs. 15 and 22), are statistically significant over much of the global land areas. The trends are fitted using the Theil–Sen Median method as a robust statistical approach.

Further details are available in the Supplementary Information and rely on refs. 62–76.

Data availability

The ALLUMs dataset is available at Zenodo (https://doi.org/10.5281/zenodo.13981586)[77]. The MCD43A3 C6.1 surface albedo data are available at https://doi.org/10.5067/MODIS/MCD43A3.061 (ref. 18) and the MCD12Q1 C6.1 LULC data from https://doi.org/10.5067/MODIS/MCD12Q1.061 (ref. 27). The MOD10A1 C6.1 daily SCF data can be obtained from https://nsidc.org/data/mod10a1/versions/61 (ref. 26). The MOD09A1 C6.1 surface reflectance data can be accessed at https://doi.org/10.5067/MODIS/MOD09A1.061 (ref. 53). The diffuse and direct surface solar radiation fluxes from the National Centers for Environmental Prediction Reanalysis Derived Products can be found at https://psl.noaa.gov/data/gridded/data.ncep.reanalysis.html. The in situ albedo observations from automatic weather station sites can be downloaded from https://doi.org/10.22008/FK2/IW73UU (ref. 61). GLASS02B03 albedo products can be obtained from https://www.glass.hku.hk/download.html. Global maps presented in this study were created using ArcGIS Pro v.2.5.0.

Code availability

The source code based on Python is available at Zenodo (https://doi.org/10.5281/zenodo.14955082)[78].

45. Hall, D. K., Riggs, G. A., DiGirolamo, N. E. & Román, M. O. Evaluation of MODIS and VIIRS cloud-gap-filled snow-cover products for production of an earth science data record. *Hydrol. Earth Syst. Sci.* **23**, 5227–5241 (2019).
46. Shepard, D. A two-dimensional interpolation function for irregularly-spaced data. In *Proc. 1968 23rd ACM National Conf.* (eds Blue, R. B. & Rosenberg, A. M.) 517–524 (Association for Computing Machinery, 1968).
47. Román, M. O. et al. Continuity between NASA MODIS Collection 6.1 and VIIRS Collection 2 land products. *Remote Sens. Environ.* **302**, 113963 (2024).
48. Kalnay, E. et al. The NCEP/NCAR 40-year reanalysis project. *Bull. Am. Meteorological Soc.* **77**, 437–472 (1996).
49. Ploton, P. et al. Spatial validation reveals poor predictive performance of large-scale ecological mapping models. *Nat. Commun.* **11**, 4540 (2020).
50. Strahler, A. H., Muller, J.-P. & Members, M. S. T. *MODIS BRDF/Albedo Product: Algorithm Theoretical Basis Document Version 5.0* (USGS, 1999).
51. Tucker, C. J. Red and photographic infrared linear combinations for monitoring vegetation. *Remote Sens. Environ.* **8**, 127–150 (1979).
52. Houldcroft, C. J. et al. New vegetation albedo parameters and global fields of soil background albedo derived from MODIS for use in a climate model. *J. Hydrometeorol.* **10**, 183–198 (2009).
53. Vermote, E. MODIS/terra surface reflectance 8-day L3 global 500 m SIN Grid V061. *NASA Earth Data* https://doi.org/10.5067/MODIS/MOD09A1.061 (2021).
54. Pendergrass, A. G., Conley, A. & Vitt, F. M. Surface and top-of-atmosphere radiative feedback kernels for CESM-CAM5. *Earth Syst. Sci. Data* **10**, 317–324 (2018).
55. Smith, C. J. et al. Understanding rapid adjustments to diverse forcing agents. *Geophys. Res. Lett.* **45**, 12023–12031 (2018).
56. Smith, C. J., Kramer, R. J. & Sima, A. The HadGEM3-GA7.1 radiative kernel: the importance of a well-resolved stratosphere. *Earth Syst. Sci. Data* **12**, 2157–2168 (2020).
57. Block, K. & Mauritsen, T. Forcing and feedback in the MPI-ESM-LR coupled model under abruptly quadrupled CO_2. *J. Adv. Model. Earth Syst.* **5**, 676–691 (2013).
58. Huang, Y., Xia, Y. & Tan, X. On the pattern of CO_2 radiative forcing and poleward energy transport. *J. Geophys. Res. Atmos.* **122**, 10578–10593 (2017).
59. Huang, H. & Huang, Y. Radiative sensitivity quantified by a new set of radiation flux kernels based on the ECMWF Reanalysis v5 (ERA5). *Earth Syst. Sci. Data* **15**, 3001–3021 (2023).
60. Liu, Q. et al. Preliminary evaluation of the long-term glass albedo product. *Int. J. Digital Earth* **6**, 69–95 (2013).
61. How, P. et al. PROMICE and GC-Net automated weather station data in Greenland. GEUS Dataverse https://doi.org/10.22008/FK2/IW73UU (2022).
62. Klein, A. & Stroeve, J. C. Development and validation of a snow albedo algorithm for the MODIS instrument. *Ann. Glaciol.* **34**, 45–52 (2002).
63. Burakowski, E. A. et al. Spatial scaling of reflectance and surface albedo over a mixed-use, temperate forest landscape during snow-covered periods. *Remote Sens. Environ.* **158**, 465–477 (2015).
64. Tedesco, M. et al. The darkening of the Greenland ice sheet: trends, drivers, and projections (1981-2100). *Cryosphere* **10**, 477–496 (2016).
65. Sun, Y., Wang, Y., Zhai, Z. & Zhou, M. Changes in the Antarctic's summer surface albedo, observed by satellite since 1982 and associated with sea ice anomalies. *Remote Sens.* **15**, 4940 (2023).
66. Ryan, J. C. et al. How robust are in situ observations for validating satellite-derived albedo over the dark zone of the Greenland Ice Sheet? *Geophys. Res. Lett.* **44**, 6218–6225 (2017).
67. Ye, F. et al. Reconstructing daily snow and ice albedo series for Greenland by coupling spatiotemporal and physics-informed models. *Int. J. Appl. Earth Observ. Geoinf.* **124**, 103519 (2023).
68. Franz, B., Kwiatkowska, E., Meister, G. & Mcclain, C. Moderate resolution imaging spectroradiometer on Terra: limitations for ocean color applications. *J. Appl. Remote Sens.* **2**, 023525 (2008).
69. Xiong, X., Sun, J., Xie, X., Barnes, W. L. & Salomonson, V. V. On-orbit calibration and performance of Aqua MODIS reflective solar bands. *IEEE Trans. Geosci. Remote Sens.* **48**, 535–546 (2010).
70. Lyapustin, A. et al. Scientific impact of MODIS C5 calibration degradation and C6+ improvements. *Atmos. Meas. Tech.* **7**, 4353–4365 (2014).
71. Bhatt, R. et al. Response versus scan-angle assessment of MODIS reflective solar bands in Collection 6.1 calibration. *IEEE Trans. Geosci. Remote Sens.* **58**, 2276–2289 (2020).
72. Angal, A., Xiong, X., Wu, A., Geng, X. & Chen, H. Improvements in the on-orbit response versus scan angle characterization of the Aqua MODIS reflective solar bands. *IEEE Trans. Geosci. Remote Sens.* **56**, 1728–1738 (2018).
73. Smith, C. J. et al. Effective radiative forcing and adjustments in CMIP6 models. *Atmos. Chem. Phys.* **20**, 9591–9618 (2020).
74. Hurtt, G. C. et al. Harmonization of land-use scenarios for the period 1500-2100: 600 years of global gridded annual land-use transitions, wood harvest, and resulting secondary lands. *Clim. Change* **109**, 117 (2011).
75. Feng, G. et al. Multiscale climatological albedo look-up maps derived from moderate resolution imaging spectroradiometer BRDF/albedo products. *J. Appl. Remote Sens.* **8**, 083532 (2014).
76. Román, M. O. et al. Assessing the coupling between surface albedo derived from MODIS and the fraction of diffuse skylight over spatially-characterized landscapes. *Remote Sens. Environ.* **114**, 738–760 (2010).
77. Hou, Z. ALLUMs. Zenodo https://doi.org/10.5281/zenodo.13981585 (2025).
78. Hou, Z. ALLUMs codes. Zenodo https://doi.org/10.5281/zenodo.14955081 (2025).

Acknowledgements This work was supported by the National Natural Science Foundation of China under grant nos. 41925006 and 42293272. G.F. was supported by the Horizon Europe Project ECO2ADAPT (grant agreement no. 101059498) and J.P. was supported by NOAA grant no. NA19NES4320002 (Cooperative Institute for Satellite Earth System Studies, CISESS) at the University of Maryland/ESSIC.

Author contributions Z.H., Liqiang Zhang, J.P., G.F., J.L., A.J. and C.Z. conceptually designed the study. Z.H., J.P., Z.Z. X.Y., S.P., H.G. and Q.W. and performed the research. Z.H., Liqiang Zhang, G.F., Z.X., Y.Q., J.L., D.J., C.Z., S.L. and Liangpei Zhang drafted the manuscript. X.Y., S.P., L. Zhao, W.F. and Z.W. analysed the data.

Competing interests The authors declare no competing interests.

Additional information

Supplementary information The online version contains supplementary material available at https://doi.org/10.1038/s41586-025-08987-z.

Correspondence and requests for materials should be addressed to Liqiang Zhang, Jintai Lin, Chenghu Zhou or Liangpei Zhang.

Peer review information *Nature* thanks Shunan Feng and the other, anonymous, reviewer(s) for their contribution to the peer review of this work. Peer reviewer reports are available.

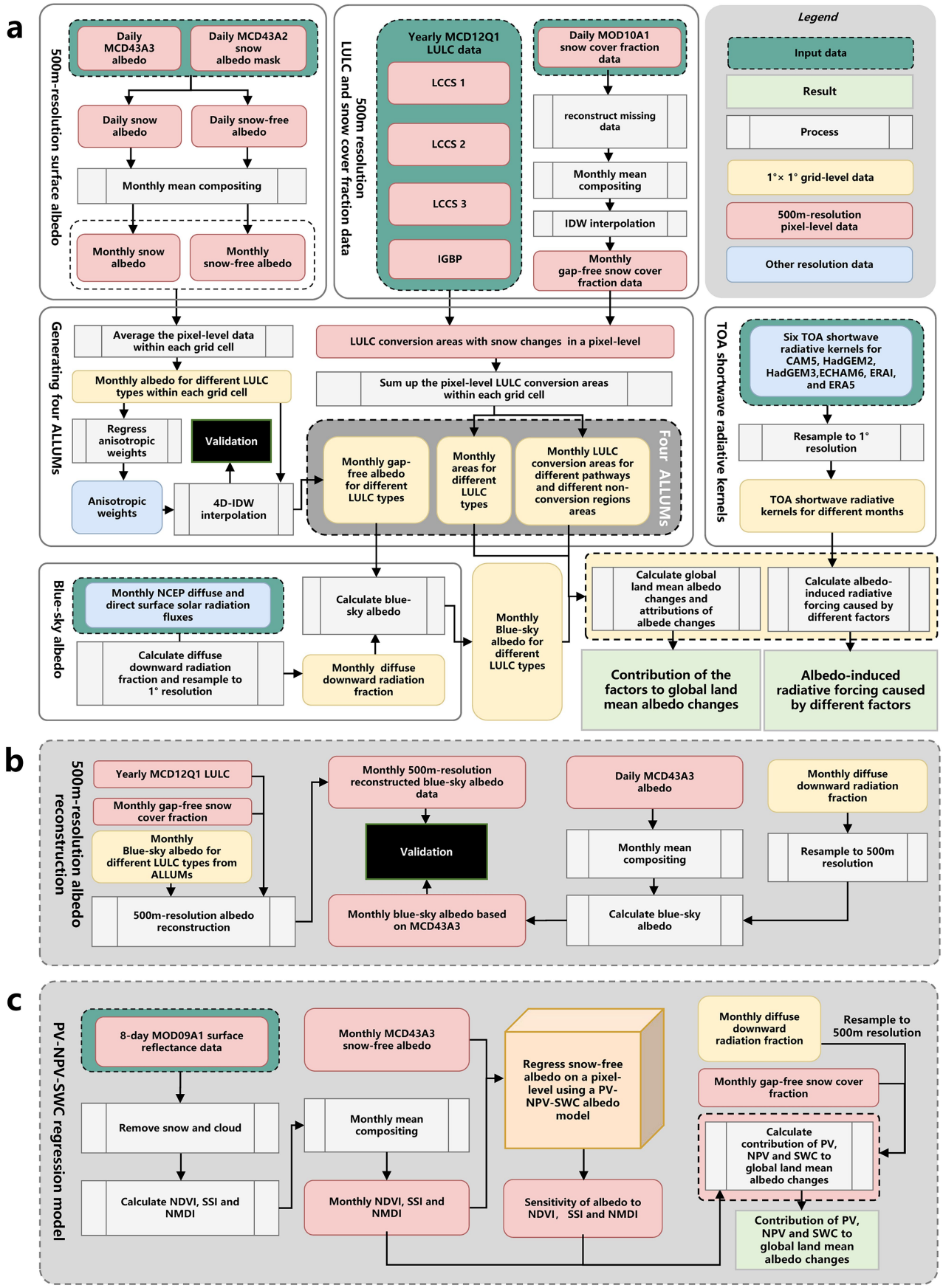

Extended Data Fig. 1 | The framework of our methodology. a, Generation of ALLUMs, and calculation of the contributions of LULC change to global land surface mean albedo change and the induced radiative forcing. **b**, Validation of reconstructed 500m-resolution blue-sky albedo. **c**, Contributions of the changes in photosynthetic vegetation (PV), non-photosynthetic vegetation (NPV) and surface water content (SWC) to albedo change over the regions without LULC conversions. The data in pink boxes and yellow boxes separately represent the 500m-resolution pixel-level data and grid-level data.

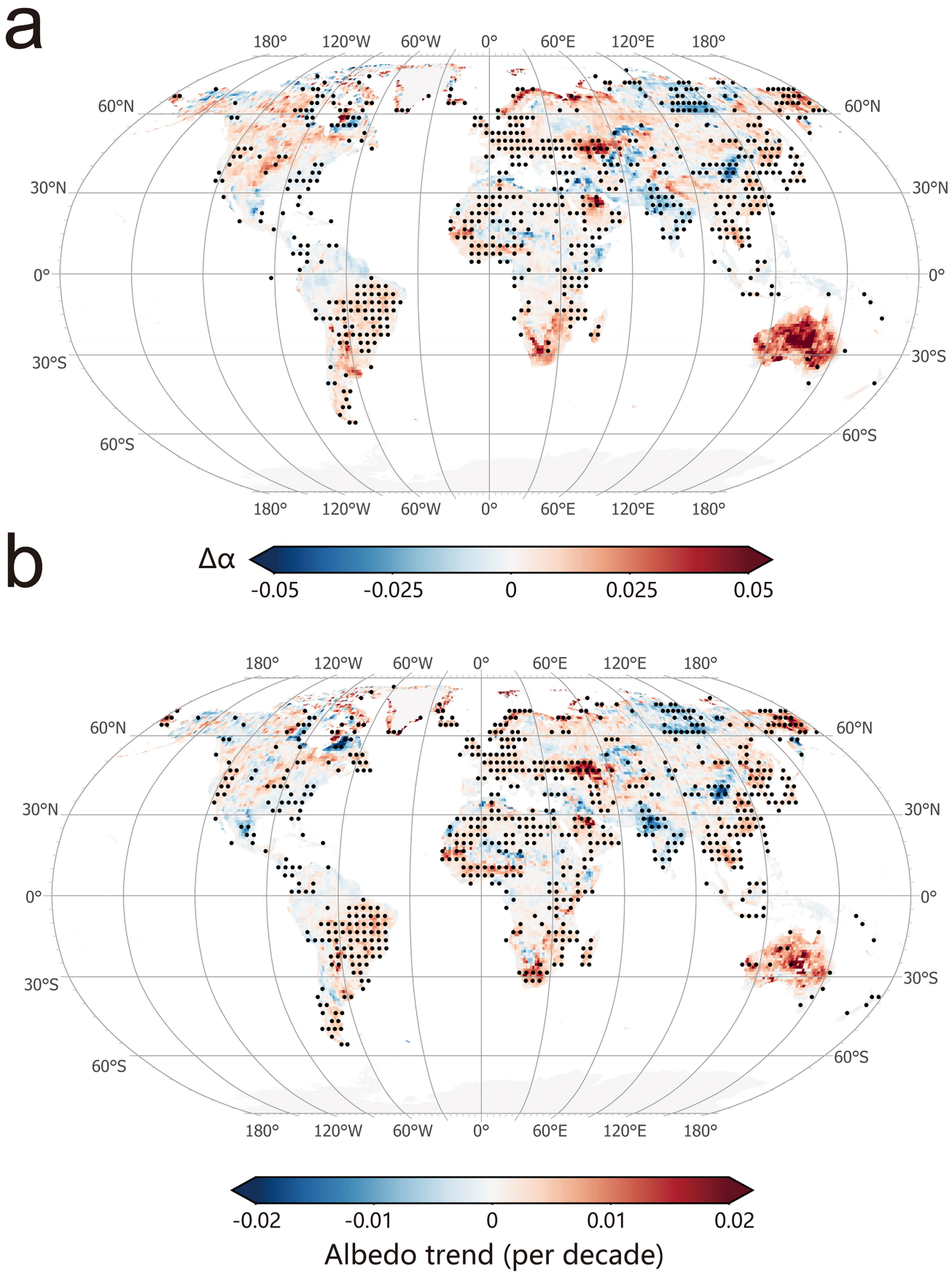

Extended Data Fig. 2 | See next page for caption.

Extended Data Fig. 2 | Spatial distribution of albedo changes in snow-free regions from 2001 to 2020. a, Absolute albedo changes from 2001 to 2020 in snow-free regions. The black dots indicate the bins where the average albedo change between two time periods (2011-2020 and 2001-2010) is statistically significant (i.e., different from zero in two-sided Student's t-test; *P*-value ≤0.05). Only the grid cells where snow-free regions account for more than 5% of the grid cell land area are displayed, and the snow-free areas with statistically significant changes account for 32.9% of all snow-free areas in these grid cells (with 24.1% showing an increase and 8.9% showing a decrease). **b**, Albedo trends in snow-free regions. The linear trend for each grid cell is regressed using the Theil-Sen Median method as a robust statistical approach. The black dots indicate statistically significant trends determined by the Mann-Kendall test (P-value ≤0.05). The snow-free areas with statistically significant trends account for 38.1% of all snow-free areas (with 29.7% showing an increase and 8.4% showing a decrease). These results represent the average albedo changes derived from ALLUM-LCCS 1-3 and ALLUM-IGBP datasets. Significance tests are conducted within each 3° × 3° grid cell for clear visualization.

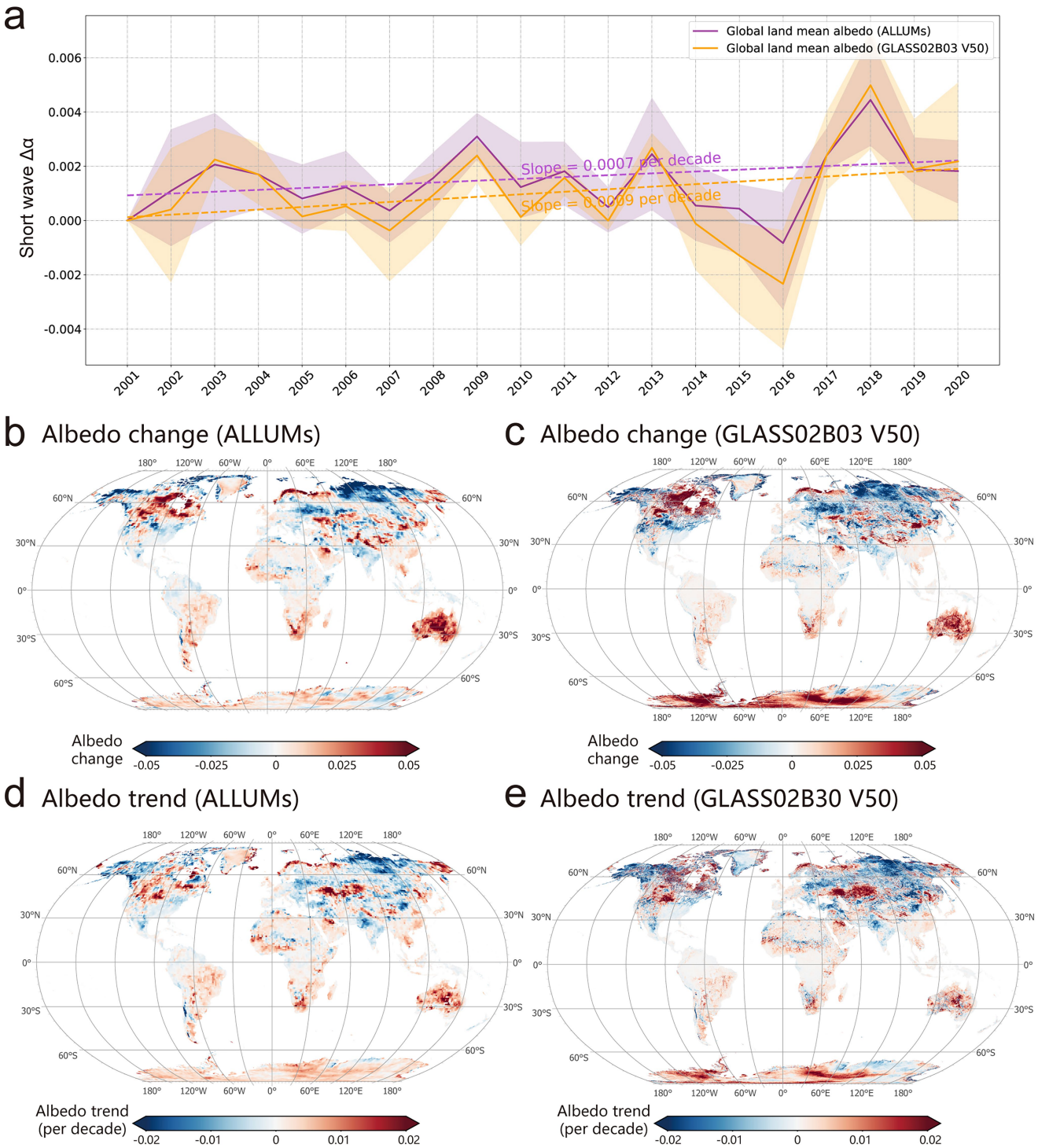

Extended Data Fig. 3 | Global land surface albedo changes based on ALLUMs and GLASS02B03. a, Annual time series of the global land surface mean albedo changes based on ALLUMs (purple line) and GLASS02B03 (orange line), respectively. Dashed lines represent the linear fits using the Theil-Sen Median method as a robust statistical approach. Shaded areas show maximum and minimum values of albedo changes of the four seasons. **b-c**, Spatial distribution of absolute albedo changes from 2001 to 2020 based on GLASS02B3 (b) and ALLUMs (c). **d-e**, Albedo trends from 2001 to 2020 based on GLASS02B3 (e) and ALLUMs (e). The Theil-Sen Median method is used to retrieve linear trends at the grid cell level. Panel (**c** and **d**) shows the average of the albedo changes calculated from ALLUM-LCCS 1-3 and ALLUM-IGBP.

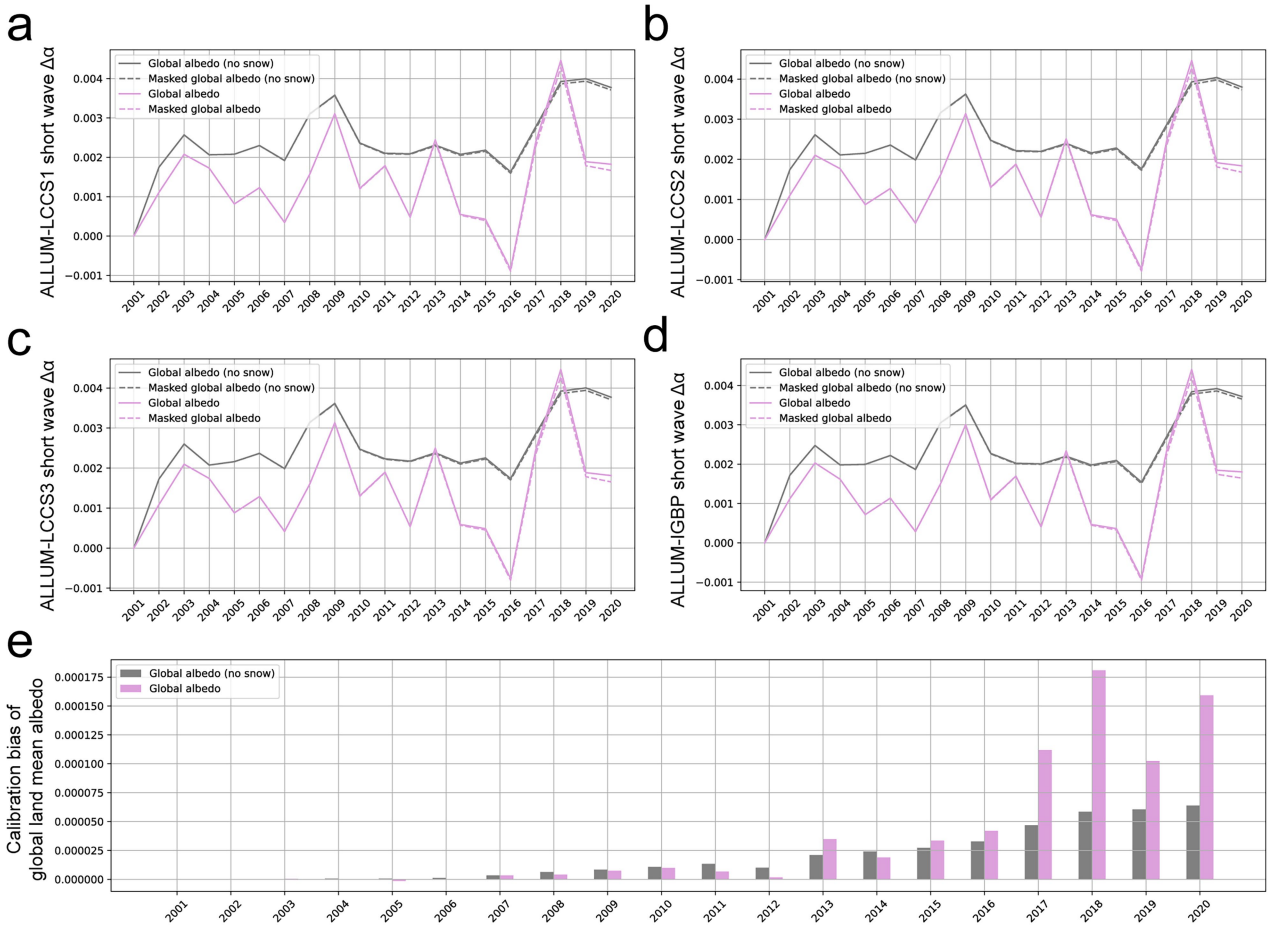

Extended Data Fig. 4 | Differences in global land surface albedo changes before and after the albedo changes smaller than the calibration limit are masked. a-d, Global land (gray line) and snow-free land (purple line) surface mean albedo changes derived from ALLUM-LCCS 1-3 **(a-c)** and ALLUM-IGBP **(d)**, respectively. The solid line and dashed line represent the differences before and after the mask. **e**, The difference in the global land surface mean albedo changes before and after the mask in the four ALLUMs is applied.

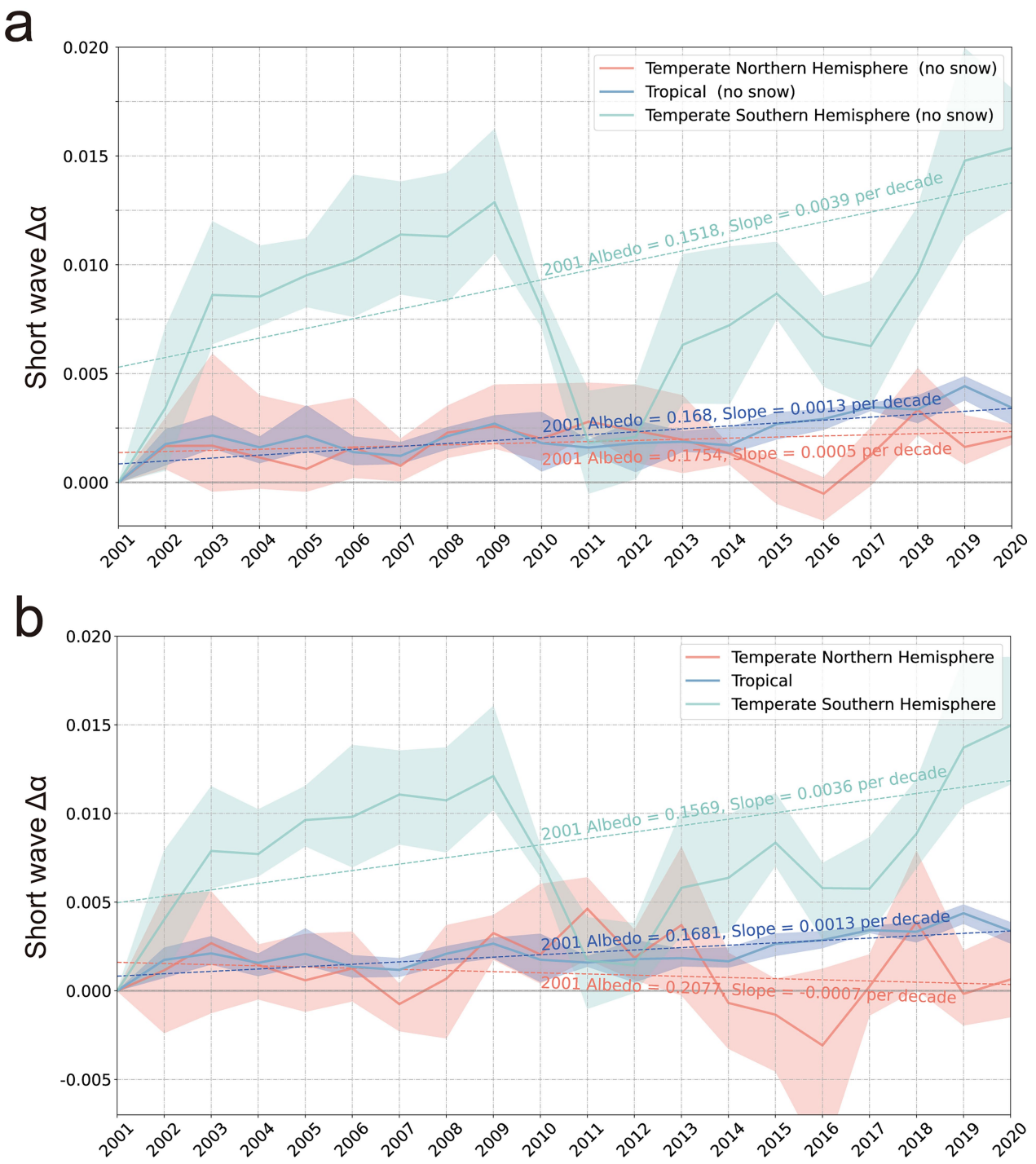

Extended Data Fig. 5 | Albedo changes in the northern temperate zone (66°N-23°N), tropical zone (23°N-23°S) and southern temperate zone (23°S-66°S). Panels (**a**) and (**b**) illustrate albedo change in snow-free regions and overall land regions (snow + snow-free regions), respectively. The shaded areas denote the maximum and minimum values of albedo change of the four seasons using the four ALLUMs. The dashed lines represent the linear fit of reflectance variation, regressed using the Theil-Sen Median method as a robust statistical approach.

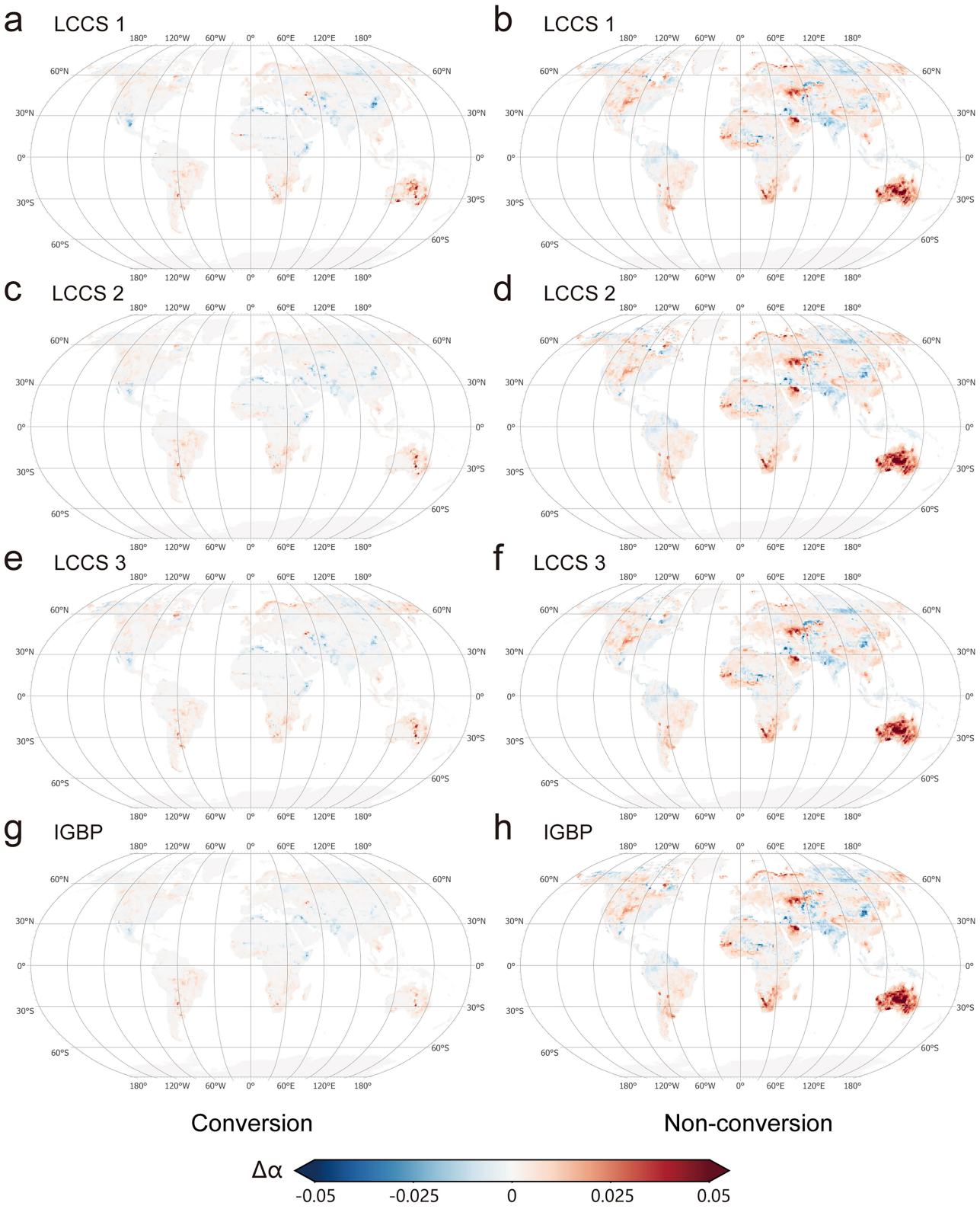

Extended Data Fig. 6 | Contributions to the land surface albedo changes from LULC conversions and non-conversion regions. The contributions of LULC conversions **(a, c, e, g)** and non-conversion regions **(b, d, f, h)** during 2001-2020 based on ALLUM-LCCS1 **(a, b)**, ALLUM-LCCS2 **(b, c)**, ALLUM-LCCS3 **(e, f)** and ALLUM-IGBP **(g, h)**.

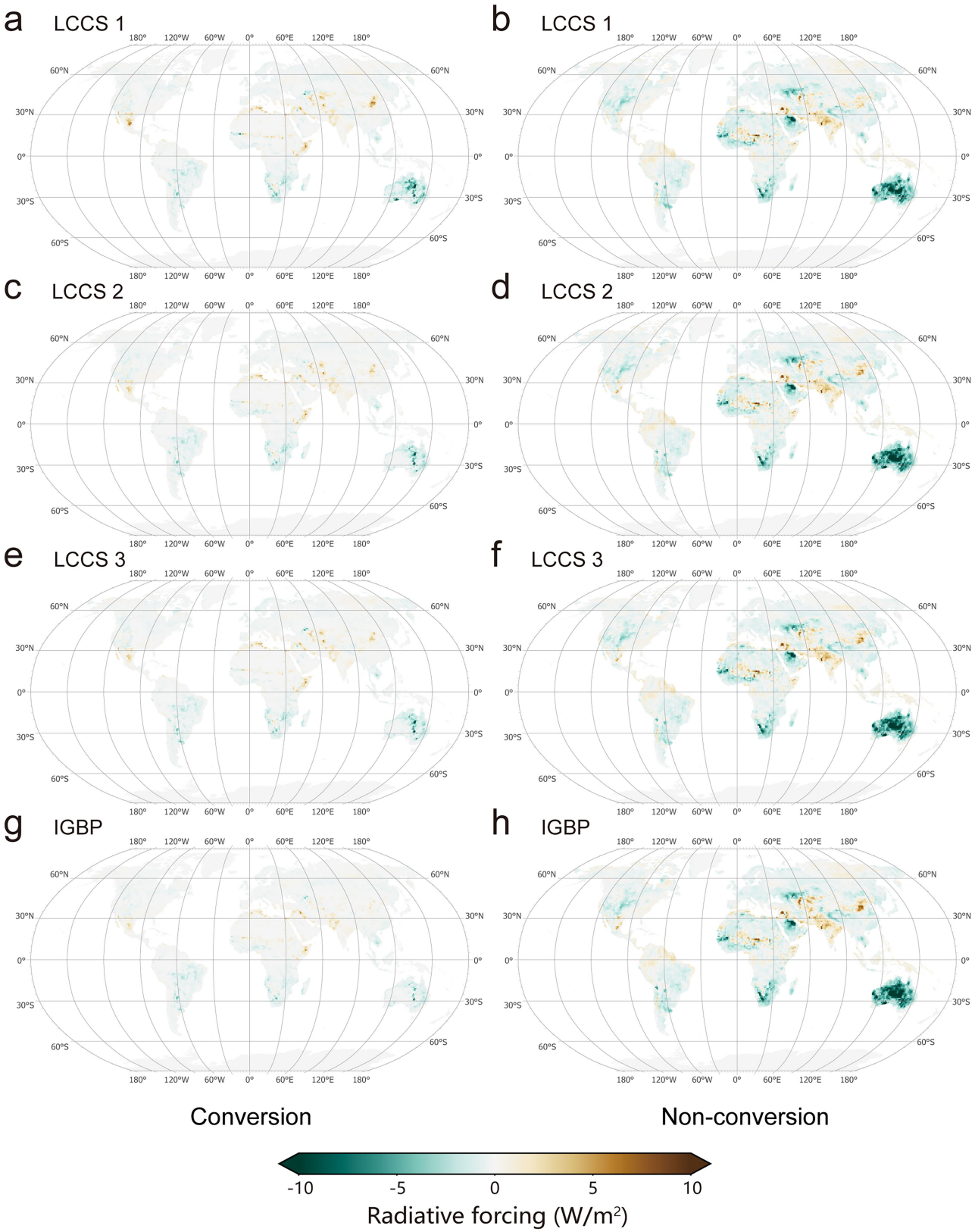

Extended Data Fig. 7 | Grid-level radiative forcing due to surface albedo changes from LULC conversions and non-conversion regions. The forcing due to LULC conversions **(a, c, e, g)** and non-conversion regions **(b, d, f, h)** during 2001-2020 based on ALLUM-LCCS 1 **(a, b)**, ALLUM-LCCS 2 **(b, c)**, ALLUM-LCCS 3 **(e, f)** and ALLUM-IGBP **(g, h)**.

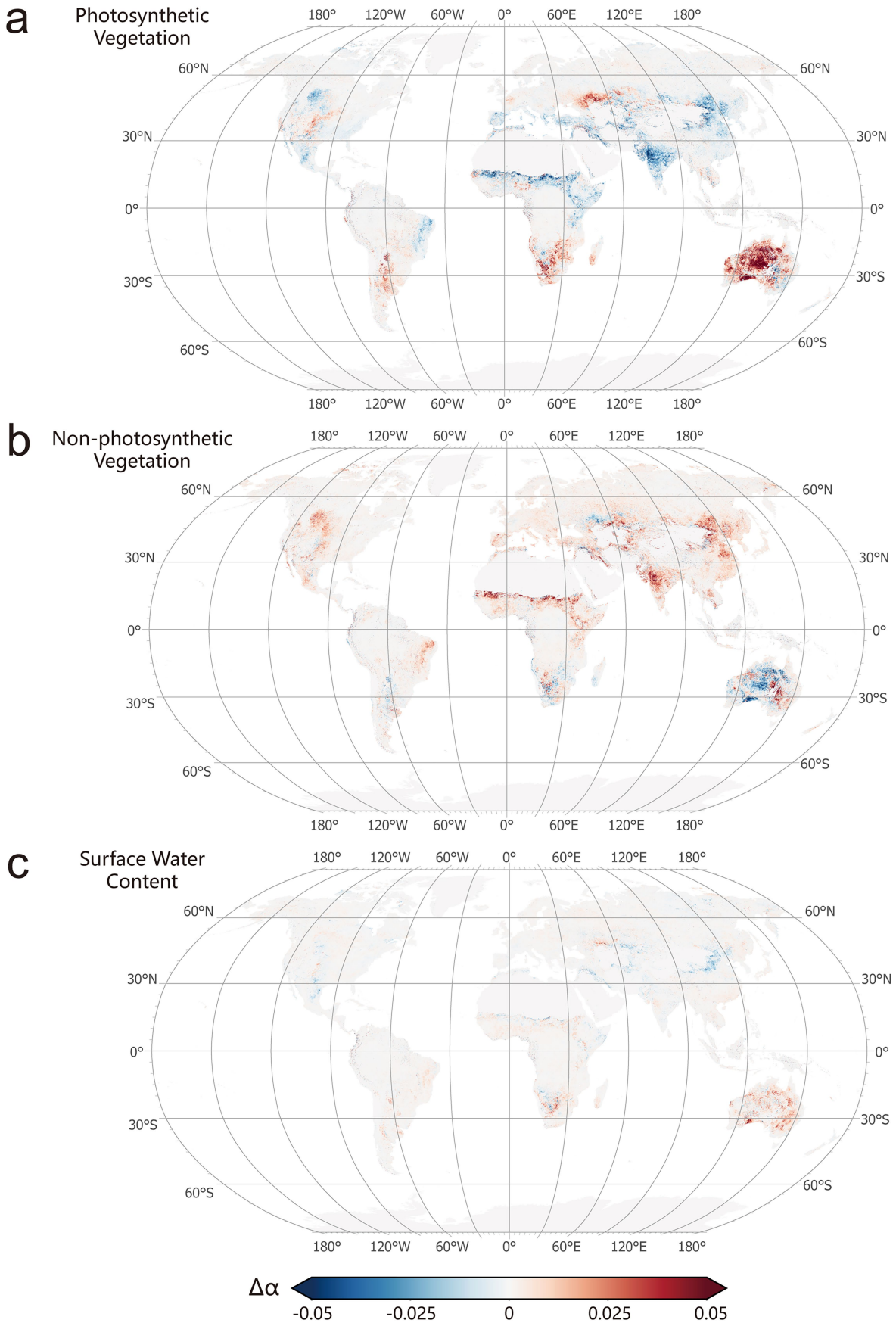

Extended Data Fig. 8 | Effects of changes in PV, NPV, and SWC on land surface albedo during 2001-2020. Panel (a), (b), and (c) illustrate the effects of changes in PV, NPV, and SWC, respectively, in LULC non-conversion regions defined by LCCS 2.

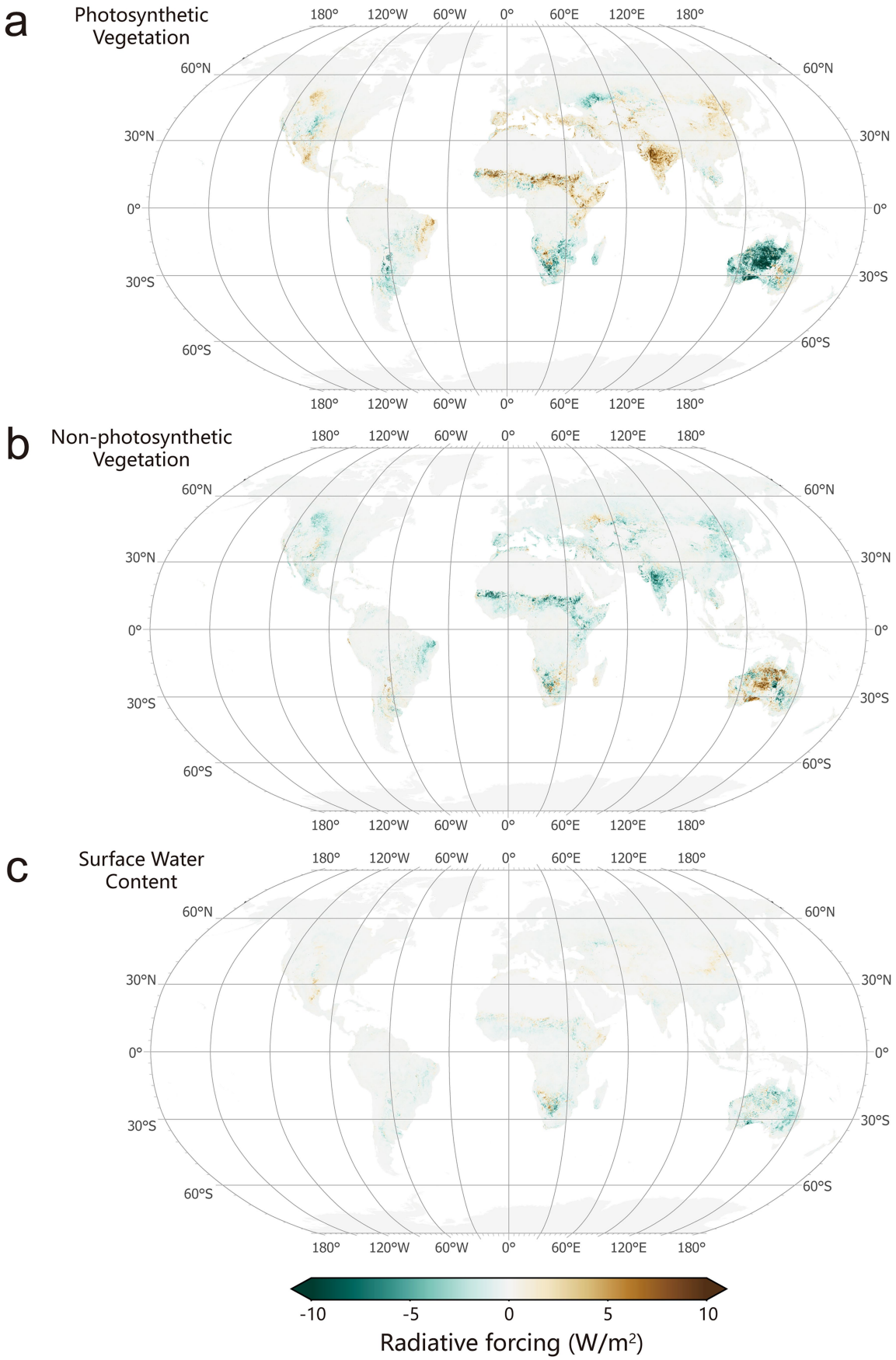

Extended Data Fig. 9 | Albedo-induced radiative forcing due to changes in PV, NPV and SWC during 2001-2020. Panel (a), (b), and (c) display the effects of changes in PV, NPV, and SWC, respectively, in LULC non-conversion regions defined by LCCS 2.

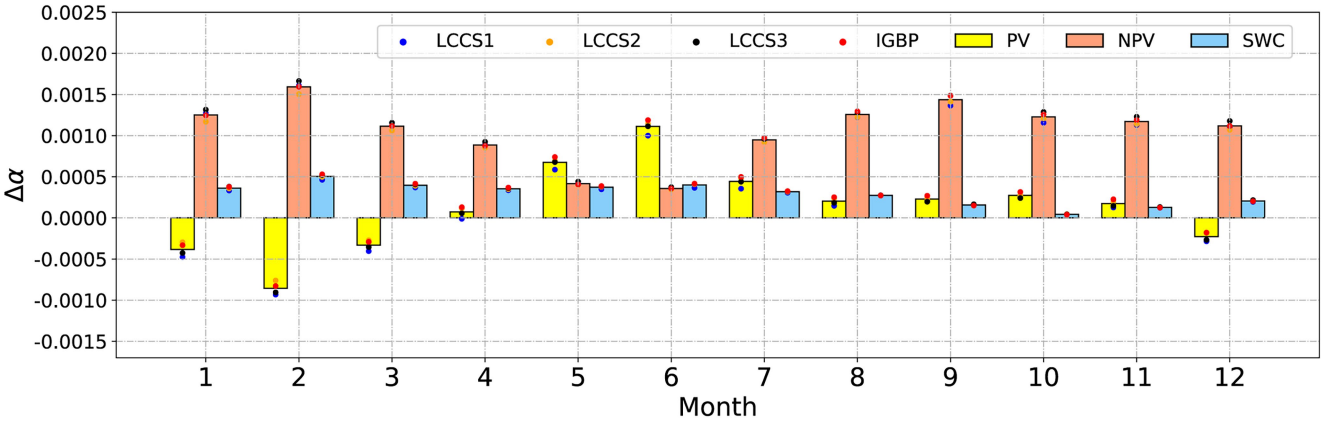

Extended Data Fig. 10 | Contributions of PV, NPV, and SWC to the monthly global land surface mean albedo change from 2001 to 2020. Points with different colors represent the results based on different LULC classification schemes. The albedo in the regions where the solar zenith angle is larger than 70° is filled with the mean in other months.